

Flow phase diagrams for concentration-coupled shear banding

S.M. Fielding^a and P.D. Olmsted^b

Polymer IRC and Department of Physics and Astronomy, University of Leeds, Leeds LS2 9JT, UK

Received 20 December 2002 and Received in final form 15 April 2003 /

Published online: 11 June 2003 – © EDP Sciences / Società Italiana di Fisica / Springer-Verlag 2003

Abstract. After surveying the experimental evidence for concentration coupling in the shear banding of wormlike micellar surfactant systems, we present flow phase diagrams spanned by shear stress Σ (or strain rate $\dot{\gamma}$) and concentration, calculated within the two-fluid, non-local Johnson-Segalman (d-JS- ϕ) model. We also give results for the macroscopic flow curves $\Sigma(\bar{\gamma}, \bar{\phi})$ for a range of (average) concentrations $\bar{\phi}$. For any concentration that is high enough to give shear banding, the flow curve shows the usual non-analytic kink at the onset of banding, followed by a coexistence “plateau” that slopes upwards, $d\Sigma/d\bar{\gamma} > 0$. As the concentration is reduced, the width of the coexistence regime diminishes and eventually terminates at a non-equilibrium critical point $[\Sigma_c, \bar{\phi}_c, \bar{\gamma}_c]$. We outline the way in which the flow phase diagram can be reconstructed from a family of such flow curves, $\Sigma(\bar{\gamma}, \bar{\phi})$, measured for several different values of $\bar{\phi}$. This reconstruction could be used to check new measurements of concentration differences between the coexisting bands. Our d-JS- ϕ model contains two different spatial gradient terms that describe the interface between the shear bands. The first is in the viscoelastic constitutive equation, with a characteristic (mesh) length l . The second is in the (generalised) Cahn-Hilliard equation, with the characteristic length ξ for equilibrium concentration-fluctuations. We show that the phase diagrams (and so also the flow curves) depend on the ratio $r \equiv l/\xi$, with loss of unique state selection at $r = 0$. We also give results for the full shear-banded profiles, and study the divergence of the interfacial width (relative to l and ξ) at the critical point.

PACS. 47.50.+d Non-Newtonian fluid flows – 47.20.-k Hydrodynamic stability – 83.10.Gr Constitutive relations

1 Introduction

For many complex fluids, the intrinsic constitutive curve of shear stress Σ as a function of shear rate $\dot{\gamma}$ is non-monotonic, admitting multiple values of shear rate at common stress. For example, Cates’ theory of semi-dilute wormlike micelles [1–3] predicts the form ACEG of Figure 1. In the regime $\dot{\gamma}_{c1} < \dot{\gamma} < \dot{\gamma}_{c2}$ of decreasing stress, steady homogeneous flow (Fig. 2a) is unstable [4]. For an applied shear rate $\bar{\gamma}$ in this unstable range, Spenley, Cates and McLeish [3] predicted that the system must separate into high- and low-shear-rate bands, $\dot{\gamma}_h$ and $\dot{\gamma}_\ell$ in Figure 2b. Any change in the applied shear rate then merely adjusts the relative fraction of the bands, while the stress Σ_{sel} (which is common to both) remains constant. The steady-state flow curve then has the form ABFG. Several constitutive models augmented with interfacial gradient terms have captured this behaviour [5–8].

Experimentally, this scenario is now well established in semi-dilute wormlike micelles [9–11]. The steady-state flow

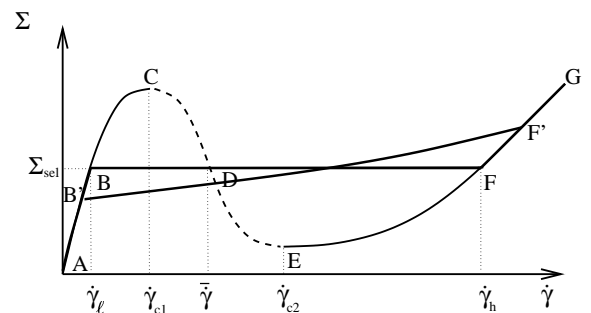


Fig. 1. Schematic flow curves for wormlike micelles: the homogeneous constitutive curve is ACEG; the steady shear-banded flow curve is BF (without concentration coupling in planar shear) or B’F’ (with concentration coupling, or in a cylindrical Couette device).

curve (often attained only after very long transients [11]) has a well-defined, reproducible stress plateau Σ_{sel} . Coexistence of high and low viscosity bands has been observed by NMR spectroscopy [10, 12–14]. Further evidence

^a e-mail: physf@irc.leeds.ac.uk

^b e-mail: p.d.olmsted@leeds.ac.uk

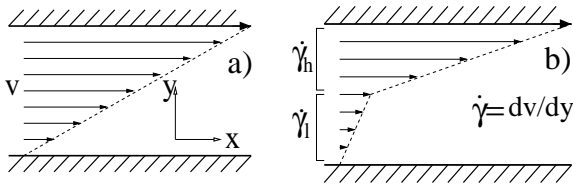


Fig. 2. (a) Homogeneous shear rate and (b) banded profiles.

comes from small-angle neutron scattering (SANS) [15–18, 9]; and from flow birefringence (FB) [19–22], which reveals a (quasi) nematic birefringence band coexisting with an isotropic one.

In some cases, the stress plateau is not perfectly flat, but slopes upward slightly with increasing shear rate: B'F' replaces BF in Figure 1. See, for example, reference [23] for the wormlike micellar solution CTAB(0.3M)/NaNO₃(1.79M)/H₂O at volume fraction $\phi = 11\%$. This effect is much more pronounced in more concentrated solutions, close to an underlying (zero-shear) isotropic-nematic (I-N) transition ($\phi \approx 30\%$) [16, 24, 15].

In a cylindrical Couette geometry, a slight upward slope B'→F' will always arise from the stress inhomogeneity due to cell curvature: as the high-shear band next to the inner cylinder expands with increasing applied shear rate into regions of lower stress, the overall applied torque must increase to ensure that the interface between the bands stays at the selected stress Σ_{sel} [5]. However, a more generic explanation of the upward slope, independent of rheometer geometry, is that the shear banding transition is coupled to concentration [25, 7], *i.e.* that a micellar concentration difference is established between the bands. In this case, the properties of each phase must change as the applied shear rate is tracked through the coexistence regime, because material is redistributed between the bands as the high-shear band grows to fill the gap.

Generically, in fact, one expects flow to be coupled to concentration in viscoelastic solutions where the different constituents (*e.g.*, polymer and solvent) have widely separated relaxation timescales [26–33]. This was explained by Helfand and Fredrickson (HF) [27] in the context of polymer solutions, as follows. In a sheared solution, parts of a stretched polymer molecule (micelle for our purposes) in regions of lower viscosity will, upon relaxing back to equilibrium, move more than the parts mired in a region of high viscosity and concentration. A relaxing molecule therefore on average moves towards the higher-concentration region. This provides a positive feedback mechanism whereby micelles can move *up* their own concentration gradient, and leads to flow-enhanced concentration fluctuations. This was observed in steadily sheared polymer solutions in the early 1990s [30]. In a remarkable paper, Schmitt *et al.* [25] discussed the implications of this feedback mechanism for the onset of flow instabilities. Following this, strongly enhanced concentration fluctuations were observed in the early time kinetics of the shear banding instability [34].

Recently, therefore, we introduced a model of concentration-coupled shear banding [35, 36] by combin-

ing the diffusive (spatially non-local) Johnson-Segalman model [37, 5] with a two-fluid approach to concentration fluctuations [26, 38–40]. This “d-JS- ϕ ” model does not address the microscopics of any particular viscoelastic system, but should be regarded as a minimal model that combines i) an unstable constitutive curve like that of semi-dilute wormlike micelles (Figure 1) with ii) spatially non-local terms in the viscoelastic constitutive equation (required for proper selection of a smoothly shear-banded state [6]), and iii) a simple approach to concentration coupling.

In references [35, 36], we examined the linear stability of homogeneous shear states in this d-JS- ϕ model with respect to coupled fluctuations in shear rate $\dot{\gamma}$, micellar strain \underline{W} and concentration ϕ to find the “spinodal”, inside which such homogeneous states are unstable. We also calculated the selected length scale at which inhomogeneity first emerges during startup flows in this unstable region. In the limit of zero concentration coupling, the unstable region coincides with that of negative slope in the homogeneous constitutive curve, as expected. Concentration coupling enhances this instability by the positive flow-concentration feedback (HF) mechanism described above, thereby broadening the region of instability, allowing crossover between “mechanical” shear banding instabilities and shear-induced demixing instabilities.

In the present paper, we compute the steady shear-banded states of the model, presenting results for the associated flow phase diagrams (the “binodals” and their tie-lines) and steady-state macroscopic flow curves. We also study the divergence of the banding interface’s width as the “critical point” of the phase diagram is approached.

We start in Section 2 by describing the experimental motivation for our work in more detail. In Section 3 we compare our calculation with the only other existing one for concentration-coupled shear banding [41]. In Sections 4 and 5, we summarize our d-JS- ϕ model, and review the results of references [35, 36] for the spinodal onset of instability. In Section 6 we describe our numerical procedure for computing steady shear-banded states, before presenting our results in Section 7. We conclude in Section 8.

2 Experimental background

In this section, we discuss in more detail the experimental evidence for concentration coupling in the shear banding of wormlike micelles. We survey both i) concentrated “prenematic” systems that are close to an underlying (zero-shear) isotropic-nematic (I-N) transition and ii) semi-dilute systems, far from this transition. In the context of these observations, in Section 3 we shall compare our work, which is aimed at the semi-dilute systems, with an earlier theoretical study of concentrated, prenematic solutions [41].

First, we review the concentrated systems. Schmitt *et al.* [16] studied CpClO₃/NaClO₃(0.05M)/H₂O at a volume fraction $\phi \approx 31\%$, just below the onset of its zero-shear I-N biphasic regime at $\phi_\ell = 34\%$. (We denote the upper boundary of this regime by ϕ_h , in the spirit of our

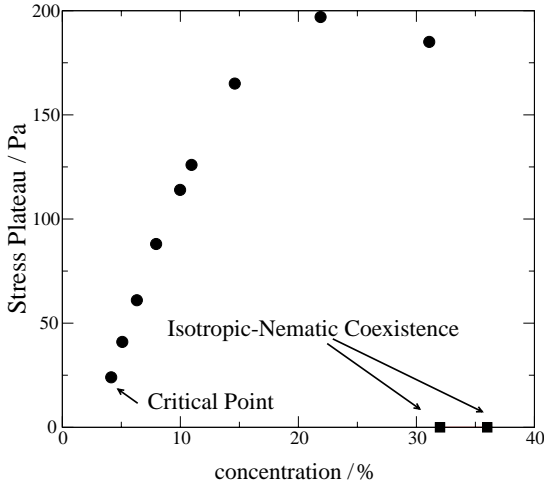


Fig. 3. Height of the coexistence plateau in the system CpCl/NaSal/brine. The 5 leftmost points are taken from the data of reference [9]. The right-hand point represents the zero-shear biphasic regime of this system, and is in accordance with the extrapolation of $G(\phi)/\Sigma_{\text{sel}}$ in reference [9] (see main text for details). We thank J.-F. Berret for providing the data for this figure.

notation $\dot{\gamma}_h$ and $\dot{\gamma}_\ell$ for the high- and low-shear bands.) In the steady-state flow curve, the stress increased markedly with shear rate throughout the banding regime, $\dot{\gamma} > \dot{\gamma}_\ell$; recall B'F' in Figure 1. As noted above, this strongly suggests a concentration difference between the shear bands, although this was not explicitly measured. Consistent with the expectation that the high-shear band should be a (shear-induced) nematic, SANS confirmed a superposition of nematic and isotropic contributions in the banding regime $\dot{\gamma} > \dot{\gamma}_\ell$, with the nematic contribution rising (linearly from zero at $\dot{\gamma} = \dot{\gamma}_\ell$) as the high-shear band expanded to fill the gap.

Berret *et al.* [15,24] studied the related system CpCl/hexanol/NaCl at a concentration just below its zero-shear I-N coexistence, $\phi \lesssim \phi_\ell \approx 32\%$. The steady-state stress was again seen to increase with shear rate throughout the shear banding regime, and accompanying SANS data now confirmed a concentration difference between the bands, with the high-shear band more highly concentrated. By studying several different (average) concentrations, the authors also showed that the stress Σ_{sel} at the onset of shear banding decreases markedly for concentrations approaching the onset of the quiescent biphasic regime, $d\Sigma_{\text{sel}}/d\phi < 0$. In particular, Σ_{sel} extrapolated to zero at $\phi \gtrsim \phi_\ell$, recovering zero-shear I-N coexistence. (This trend is shown in the rightmost points of Fig. 3.)

In view of these observations, shear banding in concentrated wormlike micelles is usually described as a shear-induced I-N transition. In contrast, banding in semi-dilute micelles (far below the zero-shear I-N coexistence regime) is usually attributed a purely mechanical origin, in the negative slope of the intrinsic constitutive curve (Fig. 1). We return to compare these two regimes in more detail in

Section 3 below. First, we review the phenomenology of the semi-dilute systems more fully.

Berret *et al.* [9] studied CpCl/NaSal/brine in the concentration range $\phi = 5\% - 20\%$, well below its I-N transition at $\phi_\ell \approx 32\%$. In this case, the banding stress Σ_{sel} was found to *increase* with increasing concentration, $d\Sigma_{\text{sel}}/d\phi > 0$. See the left 8 points in Figure 3, which start with a “critical point” ($\phi_c, \dot{\gamma}_c, \Sigma_c$), at which $\dot{\gamma}_h - \dot{\gamma}_\ell = 0$. Although this trend contrasts sharply with the concentrated systems just described, if the results for the *scaled* plateau height $\Sigma_{\text{sel}}/G(\phi)$ ($G(\phi)$ is the plateau modulus) are extrapolated to higher, prenematic concentrations, they do in fact then support the observation of $d\Sigma_{\text{sel}}/d\phi < 0$ as $\phi \rightarrow \phi_\ell$, with $\Sigma_{\text{sel}}(\phi_\ell) = 0$ [9]. (Rightmost points in Fig. 3.)

Studied across both the semi-dilute and concentrated regimes, then, the banding stress Σ_{sel} appears to be a non-monotonic function of concentration, increasing with ϕ for $5\% < \phi < 20\%$ before falling to zero in the biphasic I-N regime $\phi \approx 33\%$.

Although the results of [9] showed that shear banding in the more dilute systems depends on the solution's *overall* concentration, there is relatively little concrete evidence for concentration *coupling*, *i.e.* concentration differences between the shear bands. Indeed, the experiment just described revealed no discernible slope in the coexistence plateau for $5\% < \phi < 20\%$, and we are not aware of any explicit measurements of concentration differences between the bands. Nonetheless, recent experiments on CTAB(0.3M)/NaNO₃(1.79M)/H₂O at $\phi = 11\%$ [23] did reveal a slight upward slope in the stress plateau. And, as noted above, strongly enhanced concentration fluctuations have been seen during shear startup in such systems [34]. Along with the generic expectation that flow should be coupled to concentration in these polymeric systems [26–33], this suggests that an explicit calculation of concentration coupling in the shear banding of these semi-dilute systems might now be worthwhile. In this paper, we present the first such calculation, using our d-JS- ϕ model [35,36]. First, however, we compare and contrast our calculation with an earlier one aimed at the more concentrated, prenematic systems.

3 Theoretical context

The majority of existing calculations have assumed uniform concentration across the shear bands. An important exception is that of Olmsted and Lu [41] for shear banding in concentrated, prenematic systems. Although aimed at rigid rods rather than wormlike micelles, it broadly captured some of the phenomenology of prenematic micelles [16,15,24] described above. In particular, the stress at the onset of banding decreased with concentration, $d\Sigma_{\text{sel}}/d\phi < 0$, falling to zero in the zero-shear I-N biphasic regime, $\phi \rightarrow \phi_\ell$. The phase diagram revealed a higher concentration of rods in the high-shear (nematic) band, accompanied by an upwardly sloping coexistence plateau, $d\Sigma_{\text{sel}}/d\dot{\gamma} > 0$, in the steady-state flow curve.

To capture this shear-induced I-N transition, Olmsted and Lu explicitly assumed the orientational order parameter to be governed by a free energy that includes a nearby nematic phase. In contrast, the d-JS- ϕ model studied in this paper is aimed at systems diluted to be far below the I-N transition, and so does not have any underlying nematic feature in the elastic free energy $F^e(\underline{W})$. Instead, its shear banding instability results mainly from the non-linear convective effects of shear, via the negatively sloping constitutive curve. Nonetheless, this “mechanical” instability can be strongly enhanced by a positive feedback with concentration fluctuations, the dynamics of which are now governed by the *osmotic* free energy, $F^o(\phi)$, defined below. This feedback is particularly pronounced in systems close to an underlying Cahn-Hilliard (CH) fluid-fluid demixing transition, in which shear banding can now essentially be seen as shear-induced demixing. This crossover between i) mechanical instabilities, triggered by a negative constitutive slope and ii) shear-induced demixing instabilities was studied in detail in references [35,36]. Transferring the notion of such a crossover to the apparent dichotomy between semi-dilute and prenematic micelles, in practice there should be no sharp distinction between i) “mechanical” instabilities in the semi-dilute systems and ii) shear-induced I-N transitions in concentrated systems. The crossover between the two will be studied in a future, more sophisticated model.

4 Model

In this section we outline the d-JS- ϕ model, which couples shear banding instabilities to concentration by combining the non-local Johnson-Segalman (d-JS) model [37] with a 2-fluid framework for concentration fluctuations [26,29]. While this description is self-contained, readers are referred to reference [36] for fuller details.

4.1 Free energy

In a sheared fluid, one cannot strictly define a free energy. Nonetheless, for realistic shear rates, many internal degrees of freedom of a polymeric solution relax quickly on the timescale of the moving constraints and are therefore essentially equilibrated. Integrating over these fast variables, one obtains a free energy for a given fixed configuration of the slow variables. For our purposes, the relevant slow variables are the fluid momentum and micellar concentration ϕ (which are both conserved and therefore truly slow in the hydrodynamic sense), and the micellar strain \underline{W} that would have to be reversed in order to relax the micellar stress (slow for all practical purposes):

$$W_{\alpha\beta} = \frac{\partial R'_\alpha}{\partial \underline{R}} \cdot \frac{\partial R'_\beta}{\partial \underline{R}} - \delta_{\alpha\beta}, \quad (4.1)$$

where \underline{R}' is the deformed vector corresponding to the undeformed vector \underline{R} .

The resulting free energy is assumed to comprise separate osmotic and elastic components,

$$F = F^o(\phi) + F^e(\underline{W}, \phi). \quad (4.2)$$

The osmotic component is

$$\begin{aligned} F^o(\phi) &= \int d^3x \left[f(\phi) + \frac{g}{2} (\nabla \phi)^2 \right] \\ &\approx \frac{1}{2} \int d^3q (1 + \xi^2 q^2) f'' |\phi(q)|^2, \end{aligned} \quad (4.3)$$

where f'' is the osmotic susceptibility and ξ is the equilibrium correlation length for concentration fluctuations. The elastic component is

$$F^e(\underline{W}, \phi) = \frac{1}{2} \int d^3x G(\phi) \text{tr} [\underline{W} - \ln(\underline{\delta} + \underline{W})] \quad (4.4)$$

in which $G(\phi)$ is the micellar stretching modulus.

4.2 Dynamics

The basic assumption of the two-fluid model is a separate force balance for the micelles (velocity \underline{v}_m ; volume fraction ϕ) and the solvent (velocity \underline{v}_s) within any element of solution. The micelles are assumed to experience i) the viscoelastic stress $\delta F / \delta \underline{W} = G(\phi) \underline{W}$ acting along the micellar backbone. ii) The osmotic force $\phi \nabla \delta F / \delta \phi$ [42]. This acts directly between “monomers”, driving conventional micellar diffusion. iii) A Newtonian stress $2\phi \eta_m \underline{D}_m^0$ from fast micellar relaxation processes such as Rouse modes, where \underline{D}_m^0 is the traceless symmetric micellar strain rate tensor. We call η_m the Rouse viscosity, distinct from the zero shear viscosity of the total micellar stress. iv) The drag force, $\zeta \underline{v}_{\text{rel}}$, impeding motion relative to the solvent, $\underline{v}_{\text{rel}} = \underline{v}_m - \underline{v}_s$, where ζ is the drag coefficient. v) The hydrostatic pressure, p . Adding these, we obtain the micellar force balance equation,

$$\begin{aligned} \rho_m \phi (\partial_t + \underline{v}_m \cdot \nabla) \underline{v}_m &= \nabla \cdot G(\phi) \underline{W} - \phi \nabla \cdot \frac{\delta F(\phi)}{\delta \phi} \\ &+ 2 \nabla \cdot \phi \eta_m \underline{D}_m^0 - \zeta(\phi) \underline{v}_{\text{rel}} - \phi \nabla p. \end{aligned} \quad (4.5)$$

Likewise, the solvent experiences the usual Newtonian viscous stress, the drag force (equal and opposite to the drag on the micelles), and the hydrostatic pressure:

$$\begin{aligned} \rho_s (1 - \phi) (\partial_t + \underline{v}_s \cdot \nabla) \underline{v}_s &= 2 \nabla \cdot (1 - \phi) \eta_s \underline{D}_s^0 \\ &+ \zeta(\phi) \underline{v}_{\text{rel}} - (1 - \phi) \nabla p. \end{aligned} \quad (4.6)$$

Equations (4.5) and (4.6) contain the basic assumption of “dynamical asymmetry”, *i.e.* that the viscoelastic stress acts only on the micelles and not on the solvent [33]. Adding them, and assuming equal mass densities $\rho_m = \rho_s \equiv \rho$, we obtain the overall force balance equation for the centre-of-mass velocity, $\underline{v} = \phi \underline{v}_m + (1 - \phi) \underline{v}_s$:

$$\begin{aligned} \rho (\partial_t + \underline{v} \cdot \nabla) \underline{v} &\equiv D_t \underline{v} = \nabla \cdot G(\phi) \underline{W} - \phi \nabla \cdot \frac{\delta F(\phi)}{\delta \phi} \underline{D}_m^0 \\ &+ 2 \nabla \cdot \phi \eta_m + 2 \nabla \cdot (1 - \phi) \eta_s \underline{D}_s^0 - \nabla p, \end{aligned} \quad (4.7)$$

in which we have neglected small corrections on the left-hand side [36]. Subtracting equations (4.6) and (4.5) (with each predivided by its own volume fraction), we obtain an expression for the relative motion $\underline{v}_{\text{rel}} = \underline{v}_m - \underline{v}_s$, which in turn specifies the concentration fluctuations:

$$D_t \phi = -\underline{\nabla} \cdot \phi(1-\phi)\underline{v}_{\text{rel}} = -\underline{\nabla} \cdot \frac{\phi^2(1-\phi)^2}{\zeta(\phi)} \times \left[\frac{\underline{\nabla} \cdot G(\phi)\underline{W}}{\phi} - \underline{\nabla} \frac{\delta F}{\delta \phi} + \frac{2\underline{\nabla} \cdot \phi \eta_m \underline{D}_m^0}{\phi} - \frac{2\underline{\nabla} \cdot (1-\phi) \eta_s \underline{D}_s^0}{1-\phi} \right], \quad (4.8)$$

in which we have neglected negligible inertial corrections [36]. The essence of the two-fluid model is that the viscoelastic stress $G(\phi)\underline{W}$ appears *alongside* the familiar osmotic stress in this diffusion equation. This causes micelles to diffuse up gradients in this stress, $G(\phi)\underline{W}$, and so couples flow to concentration [27]. If the viscoelastic stress then increases with concentration ($dG/d\phi > 0$, assumed here), positive feedback occurs, causing net diffusion of micelles *up* their own concentration gradient. Although obviously opposed by the restoring osmotic force, this mechanism causes shear-enhanced concentration fluctuations and shear-induced demixing in systems already close to (zero-shear) demixing (below and Refs. [43, 26]). In shear banding systems, it causes concentration coupling (below and Refs. [35, 36, 44]).

The overall rate of micellar diffusion is set by the kinetic drag coefficient $\zeta(\phi)$. The “raw” micellar diffusion coefficient in the absence of flow-concentration coupling is $D \propto f''/\zeta(\phi)$.

For the dynamics of the viscoelastic micellar backbone strain we use the phenomenological d-JS model [37, 5]:

$$(\partial_t + \underline{v}_m \cdot \underline{\nabla})\underline{W} = a(\underline{D}_m \cdot \underline{W} + \underline{W} \cdot \underline{D}_m) + (\underline{W} \cdot \underline{Q}_m - \underline{Q}_m \cdot \underline{W}) + 2\underline{D}_m - \frac{\underline{W}}{\tau(\phi)} + \frac{l^2}{\tau(\phi)} \nabla^2 \underline{W}, \quad (4.9)$$

The terms in \underline{v}_m , \underline{D}_m and \underline{Q}_m describe convection, stretching and rotation of the micelles by flow: \underline{D}_m and \underline{Q}_m are the symmetric and antisymmetric parts of the micellar strain rate tensor, $\underline{\nabla} \underline{v}_m$. The slip parameter a measures the fractional stretch of the micelles compared to the flow. For $|a| < 1$ (slip) the intrinsic constitutive curve can be non-monotonic, as in Figure 1, capturing a shear banding instability. The term \underline{W}/τ describes relaxation of the micelles back to their unstrained state with a Maxwell time $\tau(\phi)$. The gradient term $\frac{l^2}{\tau(\phi)} \nabla^2 \underline{W}$ is discussed in Section 4.4 below.

We use equations (4.7, 4.8) and (4.9), together with the incompressibility condition, $\underline{\nabla} \cdot \underline{v} = 0$, as our model for the remainder of the paper.

4.3 Flow geometry. Boundary conditions

We consider idealised planar shear bounded by infinite plates at $y = \{0, L\}$ with $(\underline{v}, \underline{\nabla} \underline{v}, \underline{\nabla} \wedge \underline{v})$ in the $(\hat{x}, \hat{y}, \hat{z})$ directions. We allow variations only in the flow-gradient direction, \hat{y} , and so set $\partial_x \dots = 0$, $\partial_z \dots = 0$. In Appendix A we give all the relevant components of the model equations (4.7, 4.8) and (4.9) under these conditions.

The boundary conditions at the plates are as follows. For the velocity we assume there is no slip. For the concentration we assume

$$\partial_y \phi = \partial_y^3 \phi = 0, \quad (4.10)$$

which ensures (in zero shear at least) zero flux of concentration at the boundaries. Following reference [5], for the micellar strain we assume

$$\partial_y W_{\alpha\beta} = 0 \quad \forall \alpha, \beta. \quad (4.11)$$

Conditions (4.10) and (4.11) together ensure zero concentration flux at the boundary even in shear. For the controlled shear rate conditions assumed throughout,

$$\bar{\dot{\gamma}} = \int_0^L dy \dot{\gamma}(y) = \text{constant}, \quad (4.12)$$

where

$$\dot{\gamma}(y) = \partial_y v_x \quad (4.13)$$

is the local shear rate.

4.4 The interfacial terms

Spatially local models lack any information about the banding interface, and so cannot capture a smoothly banded state or a uniquely selected banding stress [8, 5, 45–47]. In contrast, the inclusion of spatial gradient terms into the viscoelastic constitutive model turns the stress selection problem into the search for a stationary “front” between the low- and high-shear-rate bands, which is only satisfied by a unique total shear stress $\Sigma = \Sigma_{\text{sel}}$ [5–7, 48, 49].

In this work, therefore, we use the non-local (“diffusive”) version of the JS constitutive model, with a spatial gradient term on the RHS of equation (4.9). (We note that other forms have been used for the gradient terms, still giving state selection [49, 50].) Although this constitutive non-locality is often disputed, such interfacial terms must always be relevant when inhomogeneities occur on microscopic scales. Physically, one can interpret this term as resulting dynamically, from the diffusion of stretched molecules across the interface [51], or statically, from nematic interactions between the micelles, or both. The length l could be set by, for example, the mesh size. However there is, at present, no detailed theory for this term in semi-dilute solutions, although Goveas and Fredrickson have considered theoretically a planar interface in polymer blends [52].

Table 1. Experimental values of the model's parameters at volume fraction $\phi = 0.11$ (column 3). Scaling laws for the dependence of each parameter upon ϕ , $Q \sim \phi^{\mu_Q}$ (column 4). In most calculations we use the reference values of column 3 at $\phi = 0.11$, then tune ϕ using the scaling laws of column 4. Only where stated do we allow the parameters to vary independently.

Parameter	Symbol Q	Value at $\phi = 0.11$	$\mu_Q = \frac{d \log Q}{d \log \phi}$
Rheometer gap	L	0.15 mm	0
Maxwell time	τ	0.17 s	1.1
Plateau modulus	G	232 Pa	2.2
Density	ρ	10^3 kg m^{-3}	0
Solvent viscosity	η_s	$10^{-3} \text{ kg m}^{-1} \text{ s}^{-1}$	0
Rouse viscosity	η_m	$0.4 \text{ kg m}^{-1} \text{ s}^{-1}$	0
Mesh size	l	$2.6 \times 10^{-8} \text{ m}$	-0.73
Diffusion coefficient	D	$3.5 \times 10^{-11} \text{ m}^2 \text{ s}^{-1}$	0.77
Drag coefficient	ζ	$2.4 \times 10^{12} \text{ kg m}^{-3} \text{ s}^{-1}$	1.54
Correlation length	ξ	$6.0 \times 10^{-7} \text{ m}$	-0.77
Slip parameter	a	0.92	0

Whereas most previous theories of shear banding have assumed uniform concentration, the concentration coupling of our model in fact provides a second source of interfacial terms, in the dynamical equation for concentration fluctuations, equation (4.8). These enter via the osmotic free energy of equation (4.3), with a lengthscale set by equilibrium correlation length ξ for concentration fluctuations. In view of this, a natural question is whether this new non-locality is itself sufficient to select a unique banding state, thereby obviating any non-locality in the viscoelastic constitutive equation. Below, we show that it is *not* sufficient.

Together, l and ξ set the length scale of any interfaces in our model. Throughout this paper, we study the physical limit in which l and ξ are small compared to the system size, $l \ll L$, $\xi \ll L$, so that we have a narrow interface connecting two bulk homogeneous phases. In this case, the solution to equations (4.7, 4.8) and (4.9) naturally fits the zero-gradient boundary conditions. A simultaneous reduction in l and ξ by the same factor then only changes the overall length of the interface, and not the values of the order parameters in each phase (which determine the phase diagram). However, the phase diagram does still depend on the ratio $r = l/\xi$ (with loss of unique selection when $r = 0$, as discussed in the previous paragraph). We will therefore give results for $r = 0, r = \infty$ and $r = O(1)$. This provides a concrete example of the early insight of Lu and co-workers [6], that the banded state must depend on the nature of the interface. This contrasts notably with equilibrium phase coexistence, for which the governing equations are integrable and therefore insensitive to interfaces.

Although we have discussed stress selection by the inclusion of non-local terms into the viscoelastic constitutive equation, a few recent works have instead invoked the equality of non-equilibrium “potentials”, within the framework of Extended Irreversible Thermodynamics (EIT) [53,54], to calculate stress selection. In this approach an extended Gibbs potential that depends on the viscous stress is assumed, with the understanding that the steady-state attractor is that state which minimizes such a

potential. This procedure then selects the banding stress. However, we maintain that such additional assumptions are unnecessary, if one is prepared to solve the full inhomogeneous profile to find the conditions of coexistence. Our assumption has instead been the reasonable one that interfacial gradients eventually introduce additional stresses into the material (this is entirely analogous to postulating a free-energy contribution that depends on the inhomogeneity of, for example, concentration or local magnetic order). Conversely, the EIT approach assumes a) that a Gibbs free energy can be defined far from equilibrium, b) that a banding state is far enough from equilibrium to necessitate such a potential, and c) that this new potential is extremized. The two methods cannot be expected to give the same results, because of the additional coefficients in the extended Gibbs potential which play no role in our treatment; moreover, there is still no reliable simple variational principle to describe strongly driven non-equilibrium fluids.

4.5 Model parameters

The d-JS- ϕ model defined above (Eqs. (4.7, 4.8, 4.9)) has the following parameters: the solvent viscosity η_s and density ρ ; the plateau modulus G ; the Maxwell time τ ; the Rouse viscosity η_m ; the mesh size l ; the osmotic modulus $f''(\phi)$ and the equilibrium correlation length ξ (recall Eq. (4.3)); the drag coefficient ζ and the slip parameter a . We also need to know the typical rheometer gap, L . A typical set of parameter values at $\phi = 0.11$ is summarised in Table 1. These values were taken from experiment or calculated using scaling arguments: see reference [36] for details. Note that explicit data is not available for $f''(\phi)$; however, dynamic light scattering gives the diffusion coefficient

$$D \equiv \frac{f''(\phi)\phi^2(1-\phi)^2}{\zeta(\phi)}. \quad (4.14)$$

In this paper we will be guided by these parameter values, but subject to the following considerations.

First, we are only interested in steady states so for convenience can consider zero Reynolds number, $\rho = 0$. For

the same reason, we can rescale the kinetic coefficient $1/\zeta$ so that the diffusion time L^2/D is of order the Maxwell time. This choice has no effect on the steady state, but make our numerical calculation of it (by evolving the *dy-namical* Eqs. (4.7, 4.8) and (4.9)) much more efficient. Second, realistic interfaces are much narrower than the typical rheometer gap, with l and ξ both $O(10^{-4}L)$. To resolve such interfaces (allowing a minimal 10 numerical mesh points per interface) would therefore require $O(10^5)$ grid points, while in practice we are limited to $O(10^2)$. We will therefore use artificially large values of l and ξ . However, this does not affect the phase diagram, provided the interface is still small compared with the gap size, as noted in Section 4.4 above. (See Sect. 6 for further details, and Fig. 5 for a typical banded profile.) Finally, we artificially increase the Rouse viscosity η_m by a factor 50 to ensure, again for numerical convenience, that the shear rate of the high shear phase is not too large. This does quantitatively change the phase diagram, but we checked that the qualitative trends are not affected.

Exploring this large parameter space is a daunting prospect so we shall not, in general, vary the parameters independently of each other. Indeed, any given phase diagram is constructed by simply tuning the single parameter ϕ (concentration), relying on known semi-dilute scaling laws for the ϕ -dependence of the other parameters (column 4 of Tab. 1). However, we will, in separate ϕ -sweeps, compute phase diagrams for different ratios of the elastic term $\nabla \cdot G(\phi) \underline{W}$ to the osmotic term $\nabla \frac{\delta F}{\delta \phi}$. We encode this degree of concentration coupling in the parameter

$$\alpha \equiv \frac{G'(\phi = 0.11)}{2f''(\phi = 0.11)} \quad (4.15)$$

(where a prime denotes a derivative with respect to ϕ). We will also investigate the dependence of the phase diagrams on the ratio of interfacial length scales, $r \equiv l/\xi$, by varying $l(\phi = 0.11)$ and $\xi(\phi = 0.11)$ in the double limit $l/L \rightarrow 0$, $\xi/L \rightarrow 0$. We adopt the convenient shorthand of l for $l(\phi = 0.11)$ with the understanding that l does actually vary with ϕ according to the scaling given in Table 1. We do likewise for ξ . Throughout we rescale stress, time and length so that $G(\phi = 0.11) = 1$, $\tau(\phi = 0.11) = 1$, and $L = 1$.

5 Intrinsic constitutive curves; spinodals

The stationary homogeneous constitutive curves (shear stress as a function of shear rate),

$$\Sigma(\bar{\gamma}, \bar{\phi}) = G(\bar{\phi}) W_{xy}(\bar{\gamma}, \bar{\phi}) + \eta(\bar{\phi}) \bar{\gamma} \quad (5.1)$$

are shown as dotted lines in Figure 4. The average viscosity $\eta(\phi) \equiv \phi \eta_m + (1 - \phi) \eta_s$. We give formulae for the components $W_{\alpha\beta}(\bar{\gamma}, \bar{\phi})$ of the micellar strain tensor in Appendix B. As the concentration $\bar{\phi}$ is reduced, the region of negative slope in the constitutive curve terminates at a “critical” point. CPCl/NaSal in brine [9] shows the same trend. In our model, this arises because decreasing

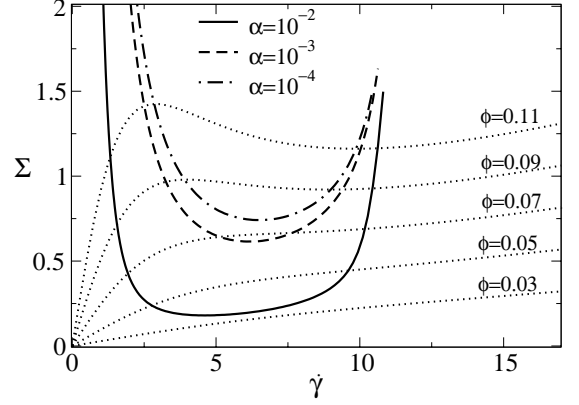


Fig. 4. Thick lines: spinodals for concentration couplings $\alpha = 10^{-2}, 10^{-3}, 10^{-4}$. Thin dotted lines: intrinsic constitutive curves for different concentrations, ϕ .

concentration reduces the viscosity of the low-shear-rate branch faster than it reduces the viscosity of high-shear-rate branch. Hence, the stress maximum decreases with decreasing concentration, and eventually vanishes.

Although these homogeneous states are *stationary* solutions of the model’s dynamical equations, they are not necessarily *stable*. In reference [35,36], therefore, we studied the dynamics of small, noise-induced fluctuations about them to find their spinodal limit of stability. The results are shown in Figure 4 for different levels concentration coupling, α . In the limit $\alpha \rightarrow 0$, fluctuations in the “mechanical variables”, \underline{W} and $\bar{\gamma}$ decouple from those in concentration, and are unstable in the region of negative constitutive slope, as expected. (Separately, the concentration could have its own Cahn-Hilliard demixing instability, when the diffusion coefficient $D < 0$. However, we are interested only in flow-induced instabilities and set $D > 0$ throughout.) For finite $\alpha > 0$, this mechanical instability is enhanced by the flow-concentration feedback described above. The region of instability is then broadened to encompass regions of positive constitutive slope, and the critical point shifts downwards.

The shear-dependent location of the isotropic-nematic spinodals in concentrated solutions of bacteriophage fd were recently studied experimentally in reference [55]. The authors interpreted their results using a Schmoluchowski equation of motion for the dynamics of the orientational order parameter under shear.

6 Numerical details

In this section, we outline our numerical procedure for solving the dynamical equations (4.7, 4.8) and (4.9). We also discuss our careful study of time-step, mesh size and finite-size effects. Readers who are not interested in these issues can skip this section.

We consider variations only in the flow-gradient direction, which we discretise $y \in [0, 1]$ on an algebraic grid $y_n = n/N_y$ for $n = 0, 1, \dots, N_y$. We stored ϕ and \underline{W} on these grid points. The velocities \underline{v}_m and \underline{v}_s were stored

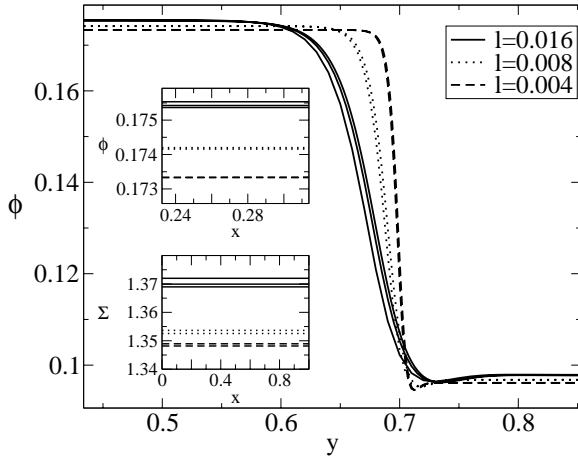


Fig. 5. Main figure: steady banded concentration profile at $\alpha = 10^{-2}$, $\xi = 0$, $\bar{\gamma} = 7.0$, $\bar{\phi} = 0.15$. Solid lines: $l = 0.016$, for $(N_y, \Delta t) = (100, 0.05), (200, 0.0125), (400, 0.0125)$, dotted lines: $l = 0.008$ for $(N_y, \Delta t) = (200, 0.05), (400, 0.003125)$, dashed lines: $l = 0.004$ for $(N_y, \Delta t) = (400, 0.05), (800, 0.05)$. Upper inset, the same data, enlarged in the left-hand phase (decreasing ϕ with increasing N_y). Lower inset: corresponding selected stresses, for the same parameter values and mesh sizes (decreasing stress with increasing N_y).

on half grid points $y_{n+1/2}$. We used a linear interpolation between the half and full grid points. We discretized time such that $t_m = m\Delta t$.

For each run, we seeded an initial profile that was either homogeneous up to a small random perturbation, or inhomogeneous according to $\phi = \bar{\phi}[1 + \Delta \cos(\pi x)]$ (with $\Delta \approx 0.1$). We then evolved the discretized equations (4.7, 4.8) and (4.9) using the semi-implicit Crank-Nicholson algorithm with centred space derivatives, under an imposed wall velocity, until a steady banded state was reached. We checked that the homogeneous phases between the interfaces (and thus the flow phase diagrams) were insensitive to the initial conditions. However, the number of bands present did depend on the initial condition: for the random initial condition several bands could form, and did not coarsen over any accessible timescale. Therefore in most runs we used the co-sinusoidal initial profile, to conveniently obtain just two bands (as in Fig. 5, for example).

For the dynamics to be independent of time-step, a very small time-step has to be used. However, the steady state is much less sensitive, allowing much larger time-steps. (As noted above, we are not interested in dynamics in this paper.) A typical steady state presented below changes by less than $10^{-3}\%$ for a factor-two reduction in time-step. For the special case of $\xi = 0$, time-steps $\Delta t \propto N_y^{-2}$ can be used, since the highest spatial derivative is second order. For $\xi \neq 0$, we have a fourth-order derivative in equation (4.8) and smaller time-steps $\Delta t \propto N_y^{-4}$ must be used.

In all our calculations, we are interested in the physical limit where the interface is much narrower than the rheometer gap. This creates a delicate balance, since a

narrow interface requires a very fine grid. Therefore, we adopted the following procedure. For any fixed value of the interfacial lengthscales l and ξ , we performed several runs with progressively finer meshes (but always with a small enough time-step) until the shear-banded profile and selected stress did not depend on the mesh. This is quite easy to achieve: a typical steady state presented below changes by less than 0.1% upon doubling the number of mesh points. We then reduced l and ξ (in fixed ratio) until the order parameters in the homogeneous phases changed by less than 0.5% upon further halving of l and ξ (but always ensuring convergence with respect to the number of grid points). A sample study of these issues is presented in Figure 5 for the special case $\xi = 0$.

7 Results

We now present our results for the steady-state flow phase diagrams, flow curves and shear-banded profiles. Because one of our aims is to show that the shear-banded state depends on the nature of the interfacial terms, we consider three separate cases: A) interfacial terms only in the viscoelastic constitutive equation (4.9) ($l \neq 0, \xi = 0, r \equiv l/\xi = \infty$); B) interfacial terms in both the constitutive and concentration equations, (4.9) and (4.8) ($l \neq 0, \xi \neq 0, r = O(1)$); and C) interfacial terms only in the concentration equation (4.8) ($l = 0, \xi \neq 0, r = 0$).

7.1 Interfacial terms only in the viscoelastic constitutive equation: $l \neq 0, \xi = 0$

In this section, we set the correlation length for concentration fluctuations, ξ , to zero and consider small but non-zero values of the interfacial lengthscale l in the constitutive equation (4.9).

7.1.1 Flow phase diagrams

For any given shear-banded profile, the values of the order parameters in each of the two homogeneous phases specify the ends of a tie line in the phase diagram. Analogous to equilibrium tie lines, the concentrations and strain rates of the coexisting states in a system with negligible interface width are related to the mean strain rate $\bar{\gamma}$ and concentration $\bar{\phi}$ by the lever rule,

$$\bar{\phi} = \beta\phi_\ell + (1 - \beta)\phi_h, \quad (7.1)$$

$$\bar{\gamma} = \beta\dot{\gamma}_\ell + (1 - \beta)\dot{\gamma}_h, \quad (7.2)$$

where β is the fraction of the gap occupied by the low-shear state $(\phi_\ell, \dot{\gamma}_\ell)$. Hence, $(\bar{\phi}, \bar{\gamma})$ lies on the tie line through $(\phi_\ell, \dot{\gamma}_\ell)$ and $(\phi_h, \dot{\gamma}_h)$.

For any given value of the concentration coupling parameter, α , we constructed the phase diagram via a succession of shear startup runs, each taken to its steady state, for average concentrations ranging from $\bar{\phi} = 0.15$ down to the critical value $\bar{\phi}_c(\alpha)$. All runs were performed at the

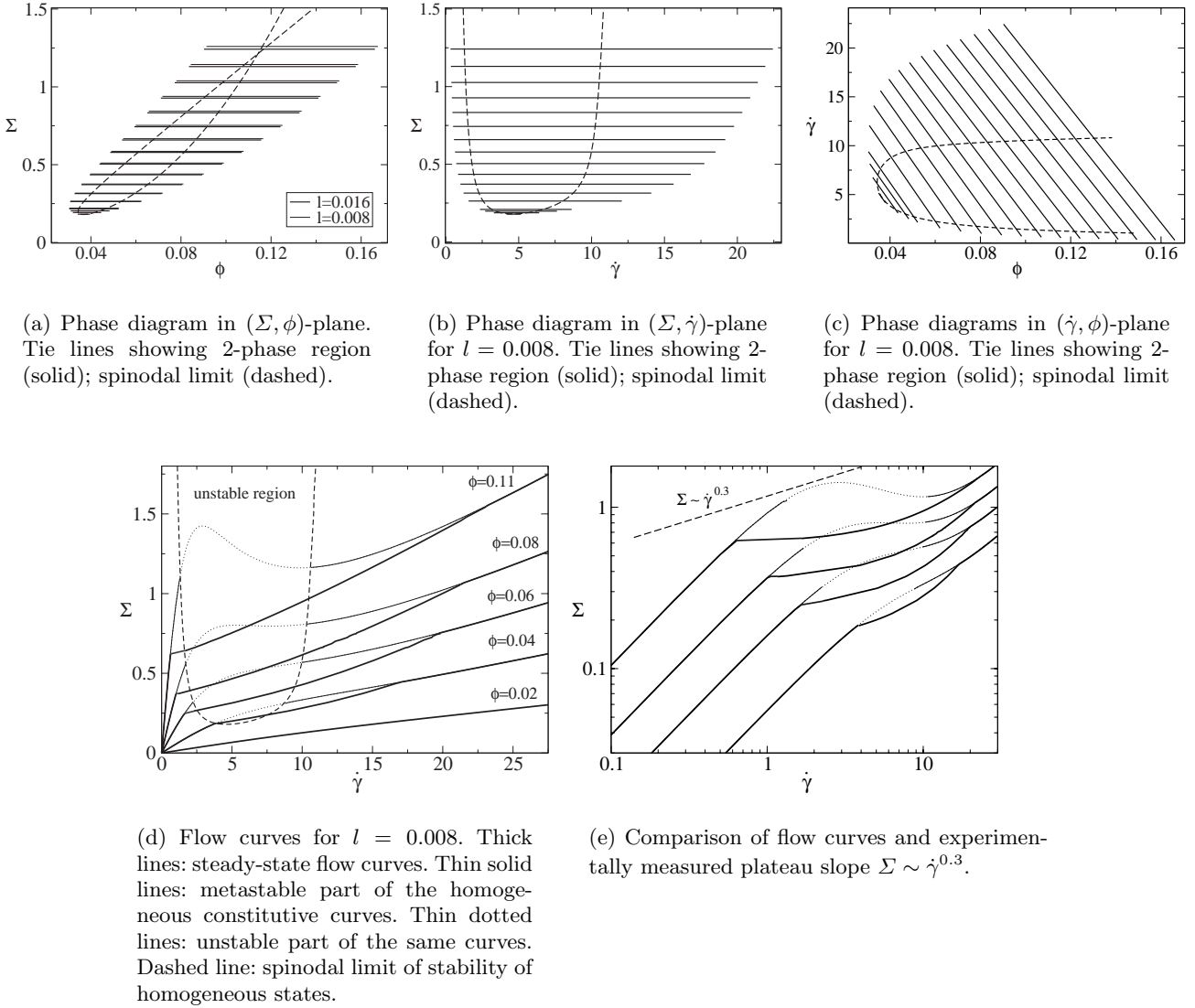


Fig. 6. Phase diagrams and flow curves for $\alpha = 10^{-2}$, $\xi = 0.0$ for small l/L . (Recall that l is actually a function of ϕ : we are using the convenient shorthand of l for the value $l(\phi = 0.11)$.) (a) Thin (upper) solid lines: tie lines for $l = 0.016$, $N_y = 100$, $\Delta t = 0.05$. Thick (lower) solid lines: tie lines for $l = 0.008$, $N_y = 200$, $\Delta t = 0.05$. As described in the main text, we actually rescaled l in the successive runs of each $\bar{\phi}$ -sweep (*i.e.* as $\bar{\phi}$ was tracked from 0.15 down to $\bar{\phi}_c$) so that the interfacial width remained (approximately) constant throughout the sweep: the value of l in the figure legends refers to the value used in the first run of the sweep, at $\bar{\phi} = 0.15$. (b,c) Solid lines: tie lines repeated in the $(\Sigma, \dot{\gamma})$, $(\dot{\gamma}, \phi)$ representations for $l = 0.008$, $N_y = 200$, $\Delta t = 0.05$. (d) Solid lines: macroscopic flow curves for $\bar{\phi} = 0.11, 0.08, 0.06, 0.04, 0.02$. These flow curves were reconstructed, using the procedure of Figure 8 below, from the tie lines of the phase diagrams (using the tie lines shown in this figure, and some additional ones). Because we have only calculated tie lines for discrete values of Σ , in some cases the reconstructed flow curves stop short of the single-phase region because of the numerical mesh, and have been continued “by eye”. (e) shows the same data, but on a log-log plot to compare with an experimentally observed slope of 0.3 (dot-dashed line). The spinodal limit is shown in each of (a-d) as a dashed line. In (d) the thin dotted lines are the unstable branches of the intrinsic (homogeneous) constitutive curves.

critical shear rate $\bar{\gamma} = \bar{\gamma}_c(\alpha)$, determined from Figure 4. Because the width, δ , of the interface in the banded state is set by l , but with a prefactor that diverges at the critical point $(\bar{\gamma}_c(\alpha), \bar{\phi}_c(\alpha))$, in each successive run we rescaled l so that δ remained (approximately) equal to its value ($\ll L$) in the first run at $\bar{\phi} = 0.15$. We return below to study the divergence of δ/l at the critical point.

The phase diagram for $\alpha = 10^{-2}$, which gives rather strong concentration coupling, is shown in Figures 6(a),(b),(c) in three different representations. The spinodal is marked in each case as a dashed line. We see from these results that the high shear phase is less concentrated than the lower shear phase, $\phi_h < \phi_\ell$: the tie lines have negative slope in the $(\dot{\gamma}, \phi)$ -plane. This

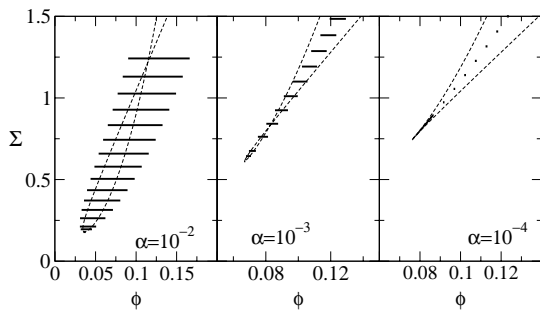


Fig. 7. Phase diagrams for three different degrees of coupling to concentration for $\xi = 0$ and small l/L . Solid lines: tie lines showing 2-phase region. Dashed lines: spinodal limit of stability of homogeneous states.

contrasts with concentrated prenematic systems, in which the high shear phase is more concentrated because flow-aligned molecules/micelles can pack more efficiently. (Recall Sects. 2 and 3 above.) This different trend seen in our model results from the HF feedback between concentration and flow. As discussed above, this feedback is captured in equation (4.8), which states that micelles tend to diffuse up gradients in the normal micellar strain component W_{yy} (where y is the flow-gradient direction). W_{yy} is more negative in the high shear phase than in the lower shear phase, since the micelles become strongly stretched along the flow direction (large W_{xx}): see the profiles of Figure 12 below. (Recall that \underline{W} describes deformation relative to the unit tensor $\underline{\delta}$.) Therefore, micelles migrate towards the low-shear band, as seen numerically.

The results of Figure 6 are for a high degree of concentration coupling $\alpha \propto G'/f''$, close to a zero-shear demixing instability (small f''). In this case, the shear banding transition sets in at quite small shear rates, and is accompanied by a large concentration difference between the bands: it has the character of “shear-induced demixing” [36]. To investigate the effect of reduced concentration coupling (further from zero-shear demixing), in Figure 7 we repeat the phase diagram for $\alpha = 10^{-2}$ alongside that for $\alpha = 10^{-3}$ and $\alpha = 10^{-4}$. As expected, the concentration difference between the bands tends to zero as $\alpha \rightarrow 0$. The coexistence regime is deferred to higher stresses and shear rates. In this case, the transition becomes a purely mechanical instability, with no concentration demixing.

Finally, to illustrate the finite-size considerations of Section 6 (above), in Figure 6(a) we showed the tie lines obtained for two different (starting) values of l . All the results shown are converged with respect to mesh fineness and time-step (not explicitly shown), but the tie lines differ slightly between the two values of l . However, all seem to be consistent with one given binodal line: we do not have any explanation for this apparent consistency.

7.1.2 Flow curves

So far, we have discussed the flow phase diagrams. Measurement of these diagrams still presents an open challenge

to experimentalists, due to the difficulty in measuring the concentration of micelles in each band (although SANS data has been used to estimate this in systems near the I-N transition [24]). However, it is important to realise that a set of flow curves $\Sigma(\dot{\gamma}, \bar{\phi})$ measured for *several* values of $\bar{\phi}$ actually contains the same information as the phase diagram. We explain how to reconstruct the phase diagram from them in Figure 8. The flow curves are relatively easily measured using conventional bulk rheology, and could therefore be used to check new measurements of concentration differences.

At any given value of $\bar{\phi}$, we calculated the flow curve as follows. We first performed a shear startup at a given $\dot{\gamma}$ in the unstable region. We then (without reinitialising the system) decreased $\dot{\gamma}$ in steps to the edge of the coexistence regime, always ensuring that a steady state was reached before measuring the total stress. We then reinitialised the system and repeated the entire procedure, but now with increasing $\dot{\gamma}$ -jumps. The results are shown in Figure 9 at the concentration $\bar{\phi} = 0.11$, for two different values of the interfacial length scale $l \ll L$. In the same figure, we also show the corresponding flow curve calculated by reversing the reconstruction procedure of Figure 8. The slight discrepancy between the directly measured flow curves and those reconstructed from the tie lines is due to the finite size of the interface $\delta \propto l$ relative to the cell L , and so is smaller for the smaller value of δ/L . The construction described in Figure 8 implicitly assumes that $\delta/L = 0$.

In Figure 6(d) we reconstructed the entire family of such flow curves, from the corresponding phase diagrams of Figures 6(a)-(c). The same data is shown on a log-log plot in Figure 6(e), to enable comparison with reference [15] in which the coexistence plateau in a log-log representation was a reasonably straight line (over the shear-rate range investigated), with slope 0.3. Note that the results shown in Figure 6(d) are in units of $G(\bar{\phi} = 0.11)$ and $\tau(\bar{\phi} = 0.11)$. In reference [56], Berret replotted the flow curves in units of $G(\bar{\phi})$ and $\tau(\bar{\phi})$, finding scaling collapse of the family $\Sigma(\dot{\gamma}, \bar{\phi})/G(\bar{\phi})$ vs. $\dot{\gamma}\tau(\bar{\phi})$ in the low-shear regime $\dot{\gamma} \rightarrow 0$. We do not find this scaling collapse (see Fig. 10) because we have used an artificially large high-shear Newtonian contribution $\eta\dot{\gamma}$ for numerical convenience (recall Sect. 4.5): the overall zero shear viscosity, $G(\phi)\tau(\phi) + \eta(\phi)$ therefore does not scale as $G(\phi)\tau(\phi)$, even approximately.

As expected for this value of α (which gives a large concentration difference between the bands; Fig. 6(a)), the steady-state flow curve “plateau” slopes strongly upwards in $\dot{\gamma}$. In Figure 11 we compare the (directly measured) macroscopic flow curve for the three levels of concentration coupling shown in Figure 7: as expected, the slope of the flow curve tends to zero with the degree of concentration coupling α .

For a shear rate at the edge of the coexistence plateau (say the lower edge), the fraction β of the gap occupied by the low shear phase becomes very small. In fact, once $\beta = O(\delta)$ (the interface width), the interface effectively touches the edge of the rheometer gap, so that we do not have a true bulk low shear phase. The stress therefore starts to deviate from the expected one. This is apparent

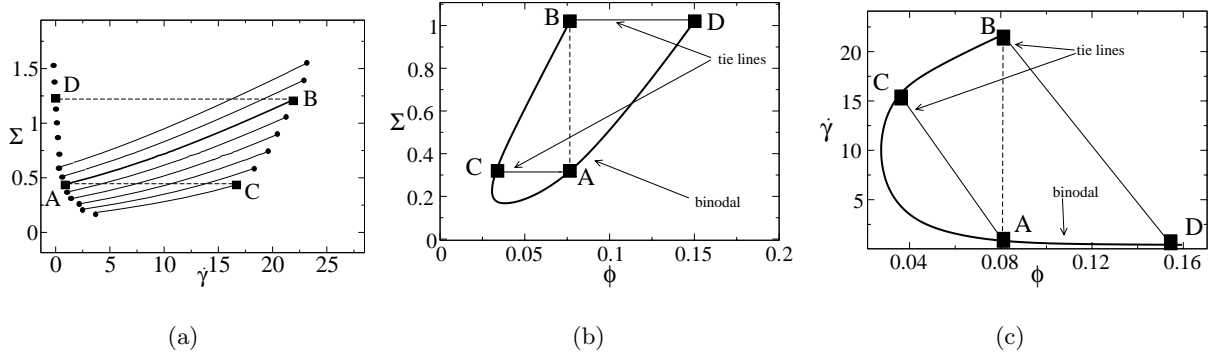


Fig. 8. Reconstruction of the flow phase diagram from a family of macroscopic flow curves $\Sigma(\dot{\gamma}, \bar{\phi})$, measured for several different average concentrations $\bar{\phi}$. Consider the flow curves of (a). The curve that starts at A and ends at B in (a) is for an average concentration $\bar{\phi} = 0.08$. This specifies the corresponding points A and B in (b), (c). Repeating this for all the circles in (a), we can construct many points on the binodal in (b) and (c), which can then be interpolated between to give the full binodal. We now just need to specify the tie lines. In (b) this is trivial: all tie lines are horizontal since the coexistence occurs at common stress (for gradient banding). In (c), to get the slope of the tie line that starts at B we proceed by recalling that the tie line represents constant shear stress. Therefore we find the point D in (a) that is at the same stress as point B, and read off its average strain rate. Its average concentration is already known. This gives point D in (c). Similarly, A is the image of point C at constant stress. Repeating this process we can fill in all the tie lines of the phase diagram.

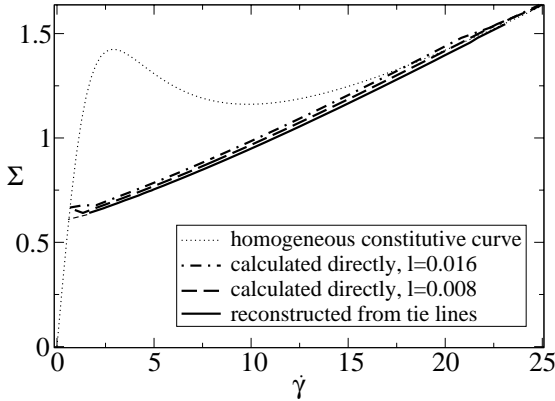


Fig. 9. Macroscopic inhomogeneous flow curves for $\alpha = 10^{-2}$ at $\phi = 0.11$. Thick solid line: reconstructed, from the tie lines of the phase diagram. Dot-dashed and dashed lines: calculated by directly measuring the average stress and strain rate during a strain rate sweep for $l = 0.016$, $N_y = 100$, $\Delta t = 0.05$ (dot-dashed) and $l = 0.008$, $N_y = 200$, $\Delta t = 0.05$ (dashed). (The slight discrepancy between these three curves is discussed in the text.) The thin dotted line is the intrinsic (homogeneous) constitutive curve.

at the lower binodal for $\alpha = 10^{-2}$ in Figure 11. (Only one of the shear rates used happened to fall in this “boundary” range.) However, we expect this (steady-state) effect to be much less pronounced in experimental systems, since realistic interfaces are much smaller than those used in our numerical study. Only near a critical point, where the interface becomes very broad (for fixed l), would we expect to see a true steady-state bump at the edge of the plateau. Nonetheless, pronounced bumps are often apparent in flow curve data obtained via upward strain rate sweeps. However, this has a different origin: the high-shear band cannot

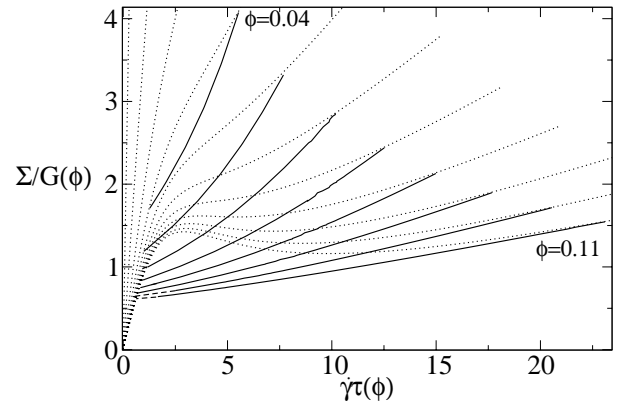


Fig. 10. Macroscopic flow curves as shown in Figure 6(d) above, but now with the stress in units of $G(\phi)$ and the strain rate in units of $\tau(\phi)$.

nucleate on the timescale of the sweep, so that the system departs up the metastable part of the homogeneous low-shear branch. In this case the stress bump is metastable, and can be eliminated (or at least reduced) by reducing the rate of the sweep [11,5].

As noted in Section 1, in a curved Couette geometry the “plateau” in the flow curve (B’F’ of Fig. 1) will slope upwards due to the inhomogeneity of the stress field, even without concentration coupling. It should be noted that all calculations in this paper are for a planar shear geometry, and the slope of our flow curves in the coexistence regime results solely from concentration coupling. In fact, the slope in Figure 6(d) is far greater than one would typically expect from curvature effects alone: for a Couette cell with radius R and gap δR , the stress measured at the inner Couette wall would change by $\delta\Sigma/\Sigma = 2\delta R/R$ over the coexistence regime, and so too would the relative

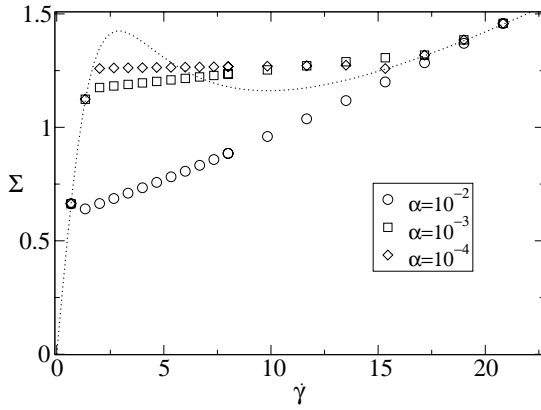


Fig. 11. Macroscopic inhomogeneous flow curves for three different degrees of coupling to concentration. Each is calculated from direct measurement of the stress under a strain rate sweep at fixed $\bar{\phi}$.

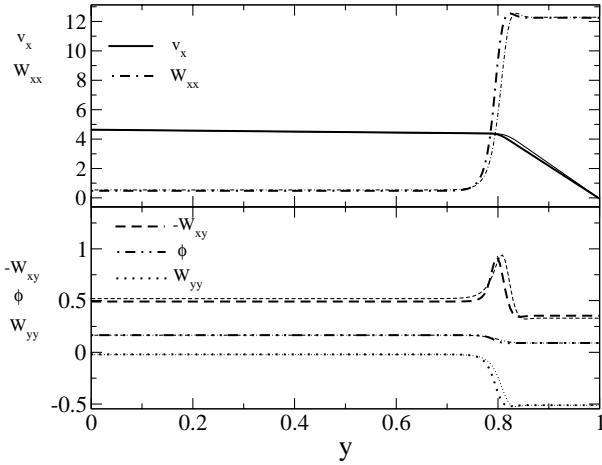


Fig. 12. Steady-state shear-banded profile at $\alpha = 10^{-2}$, $\bar{\gamma} = 4.64$, $\bar{\phi} = 0.15$ for two different ratios $r = l/\xi$. The thick lines are for $r = \infty$ ($l = 0.008$, $\xi = 0.0$), $N_y = 200$, $\Delta t = 0.05$, as considered in this section. The thin lines show the corresponding results for $r = 0.4$ ($l = 0.008$, $\xi = 0.002$), $N_y = 200$, $\Delta t = 0.00625$ (discussed in Sect. 7.2), for comparison.

change in torque through the coexistence “plateau”. The slope of Figure 6(d) would therefore require an atypically large curvature of $\delta R/R \sim 0.5$.

7.1.3 Interfacial profiles; divergence of interface width at the critical point

We now turn to the interfacial profiles. A full steady-state banded profile for $\alpha = 10^{-2}$ (corresponding to the right-most/uppermost tie line in Fig. 6(a),(b),(c)) is shown by the thick lines in Figure 12. As required, the interface is smooth on the scale of the mesh, but narrow on the scale of the gap size, *i.e.* $L/N_y \ll \delta \ll L \equiv 1$, where δ is the width of the interface. Note that the shear rate is negative across the gap since we have chosen the wall at $y = 0$ to be the one that moves: $v_x(y = 0) = \bar{\gamma}L$. Accordingly, we have plotted $-W_{xy}$, since W_{xy} is antisymmetric in shear

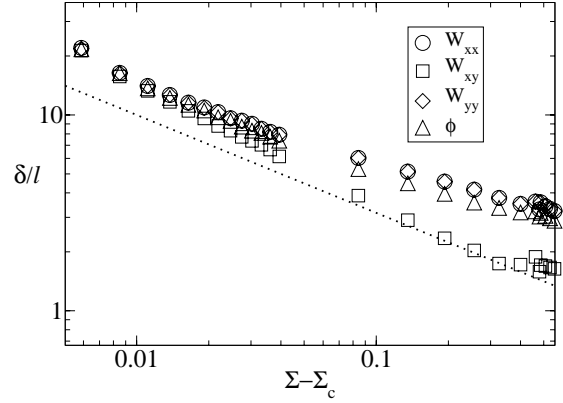


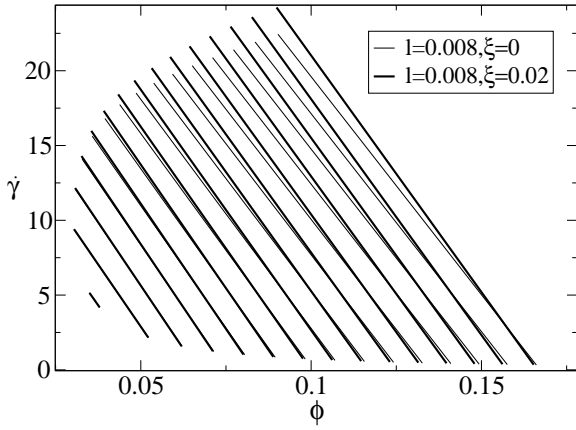
Fig. 13. Scaled interface width δ/l vs. the distance from the critical stress $\Sigma - \Sigma_c$. The dotted line shows $\delta \sim (\Sigma - \Sigma_c)^{-0.5}$.

rate. $-W_{xy}$ is rather small in the high-shear band, as expected from the underlying constitutive non-monotonicity. Meanwhile, W_{xx} is very large, while $W_{yy} \approx -0.5$. (Recall that \underline{W} measures deformation relative to the unit tensor $\underline{\delta}$.) This corresponds to the strongly sheared micelles being highly stretched along the flow direction, consistent with the experimental observation that the first normal stress difference increases throughout the banding regime [18]. The concentration is lower in the high-shear band, where W_{yy} is smaller (more negative), due to the Helfand-Fredrickson mechanism described above.

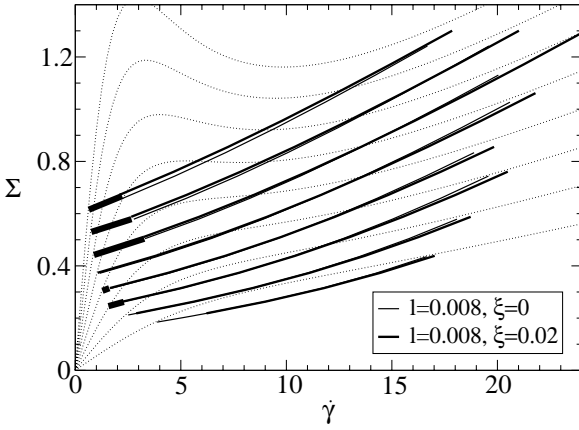
The interface width, δ , is actually slightly different for each order parameter. In each case, we define it to be the distance between the two points where the change in that order parameter between the two homogeneous phases is 25% and 75% complete. For a fixed value of l (which sets the overall scale of the interface width), δ diverges at the critical point (for each order parameter). In tracking $\bar{\phi}$ down towards the critical point, therefore, we continually rescaled l to ensure that the interface width remained approximately constant, as discussed above. In each case, we measured δ/l , for each of W_{xy} , W_{xx} , W_{yy} and ϕ : see Figure 13. According to mean-field theory, the divergence should be of the form $\delta/l \sim (\Sigma - \Sigma_c)^{-1/2}$. The power $-1/2$ is therefore shown as a guide for the eye in Figure 13.

7.2 Interfacial terms in both the viscoelastic constitutive equation, and in the concentration equation: $l \neq 0$, $\xi \neq 0$

We now study the effect of including interfacial gradient terms in the concentration equation (4.8) as well as in the viscoelastic equation (4.9), so that now $\xi \neq 0$ as well as $l \neq 0$. Hence, while in the previous section we considered $r \equiv l/\xi = \infty$, we now consider $r = O(1)$. In Figure 14(a), we give the phase diagram for $r = 0.4$. Comparing it with our results for $r = \infty$ (also shown in Fig. 14(a)), we see that the slopes of the tie lines and the overall binodal both depend quantitatively on r . (This difference between the results for $r = \infty$ and $r = 0.4$ is far greater than any



(a) Tie lines.



(b) Partially reconstructed macroscopic flow curves (solid); homogeneous constitutive curve (dotted). The very thick solid lines at the left-hand side are a continuation of the data by eye to the edge of the coexistence regime.

Fig. 14. Comparison of phase diagrams and flow curves for $\alpha = 10^{-2}$, $r = 0.4$ ($l = 0.008$, $\xi = 0.02$) with those for $\alpha = 10^{-2}$, $r = \infty$ ($l = 0.008$, $\xi = 0$).

“error” associated with the fact that numerically we cannot truly attain the limit $\Delta t \rightarrow 0$, $lN_y \rightarrow \infty$, $\xi N_y \rightarrow \infty$, $l/L \rightarrow 0$ and $\xi/L \rightarrow 0$.) This provides a concrete example of the fact that shear banding coexistence is determined by, and non-universal with respect to, the interfacial terms [6]. As noted above, this contrasts sharply with the equilibrium case, in which the equations of motion are integrable and the phase diagram independent of the interfacial terms. Although conceptually important, this dependence is in practice rather weak in our model: the overall features of the phase diagram are unchanged. Moreover, the critical point is truly unaffected. In Figure 14(b) we show the corresponding macroscopic flow curves, reconstructed using the tie lines of Figure 14(a). The slight difference between $r = \infty$ and $r = 0.4$ is again apparent.

Figure 12 compares the full banded profiles for $r = \infty$ and $r = 0.4$.

7.3 Interfacial gradient terms only in the concentration equation: $l = 0$, $\xi \neq 0$: loss of state selection

7.3.1 Numerical results

Finally we set the interfacial length l in the constitutive equation (4.9) equal to zero, $r \equiv l/\xi = 0$. The constitutive equation is now local, so the only source of spatial gradients in the model is the equilibrium correlation length for concentration fluctuations, ξ (Eqs. (4.8) and (4.3)). In the absence of concentration coupling, $\alpha = 0$, it is known that there is no uniquely selected, smoothly shear-banded state in this case, $l = 0$ [6]. Here we investigate whether a smoothly banded state is selected for $\alpha \neq 0$, by virtue of the interfacial terms in the concentration equation.

Numerically, we were only able to obtain a smoothly banded profile for stresses near the critical point. At larger stresses, the profiles were spiky, even for the largest accessible values of ξ and N_y . See Figure 15(b). The tie lines corresponding to the smooth profiles are shown in Figure 15(a), alongside the corresponding results at $r = 0.4$ for comparison. Consistent with the discussion of non-universality in the previous section, the (smoothly banded part of the) phase diagram for $r = 0.0$ is slightly different from that for $r = 0.4$ (and is different again from the case $r = \infty$; not shown).

The binodal formed by the tie lines associated with the spiky profiles (not shown in Fig. 15(a)) is irregular, suggesting that the steady state is not uniquely selected. Figure 15(c) provides further evidence of this, showing that the steady state depends on the initial condition. In view of this, a natural question is whether selection could occur in principle (but is inaccessible with any realistic mesh due to the pronounced non-monotonicity in $W_{xy}(y)$), or whether it is truly lost. We now present an analytical argument showing the latter, selection loss for $l = 0$.

7.3.2 Selection loss

Looking back at the model’s dynamical equations (Sect. 4; expanded componentwise in App. A), we see that in steady state the system must obey:

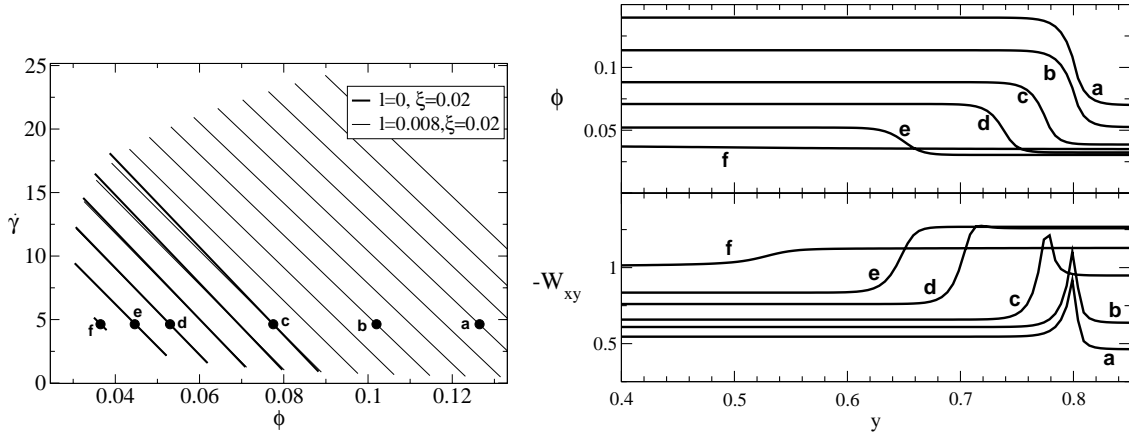
1. The x -component of the force-balance equation (Eq. (4.7)), equivalent to equation (A.1) [57]:

$$S(\dot{\gamma}, \phi) \equiv G(\phi)W_{xy}[\dot{\gamma}\tau(\phi)] + \bar{\eta}(\phi)\dot{\gamma} = \Sigma = \text{const.} \quad (7.3)$$

2. The (now local) constitutive equation (Eq. (4.9)), equivalent to equations (A.6),

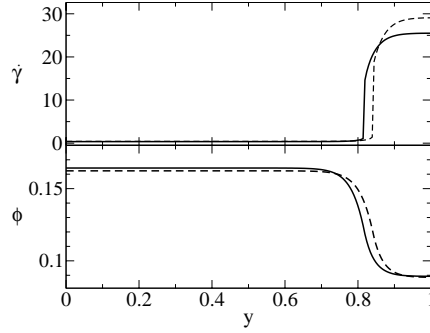
$$W_{\alpha\beta} = W_{\alpha\beta}[\dot{\gamma}\tau(\phi)] \quad \text{for } \alpha\beta = xx, xy, yy. \quad (7.4)$$

Substituting W_{xy} from equation (7.4) into equation (7.3), we obtain the family of homogeneous constitutive curves $S(\dot{\gamma}, \phi)$, plotted in Figure 4 above. Because the constitutive relation is now local, the solution at all points across



(a) Tie lines, only shown for the case $l = r = 0$ when close to the critical point.

(b) Steady-state profiles for initial condition $\phi(y) = \bar{\phi} + 0.4 \cos(\pi y)$, for points a–f in (a). There is no selected smoothly banded state for points a, b, and c.



(c) Steady-state profiles for initial conditions $\phi(y) = \bar{\phi} + 0.4 \cos(\pi y)$ and $\phi(y) = \bar{\phi} + 0.7 \cos(\pi y)$: the steady state depends on the initial condition.

Fig. 15. (a) Phase diagram at $\alpha = 10^{-2}$, for $l = 0.0$, $\xi = 0.02$, $r \equiv l/\xi = 0.0$, shown with the corresponding data for $l = 0.008$, $\xi = 0.02$, $r = 0.4$ for comparison. Tie lines are only shown near the critical point because for larger values of $\bar{\phi}$, there is no uniquely selected, smoothly banded state. This is shown in (b) and (c). (c) shows the steady-state profiles in $\phi(y)$ and $\dot{\gamma}(y)$ for $\bar{\phi} = 0.16$ and $\bar{\gamma} = 4.66$ with initial condition $\phi_0(y) = \bar{\phi} + 0.4 \cos(\pi y)$ (solid lines) and with $\phi_0(y) = \bar{\phi} + 0.7 \cos(\pi y)$ (dashed lines). Since the “selected” state depends upon the initial condition (c) and yields a non-analytic profile in W_{xy} (b), we conclude that there is no state selection for $l = 0$ for stresses far enough above the critical point (see the text for a discussion).

the rheometer cell must lie on one of these curves. Indeed, as the shear rate changes across the interface, the system must pass through constitutive curves of differing concentrations to maintain a uniform stress, $\partial_y \Sigma = 0$. In other words, a relation $\phi = \phi(\dot{\gamma}, \Sigma)$ must be obeyed. The family of these curves is shown as dotted lines in Figure 16(a). The regime of non-monotonicity in ϕ vs. $\dot{\gamma}$ is a direct result of the non-monotonicity in S vs. $\dot{\gamma}$.

As well as the force balance and constitutive equations, the system must also obey

3. The concentration equation (Eq. (4.8)), equivalent to equation (A.9), in which we can set $v_{my} = v_{sy} = 0$ in

the steady state:

$$0 = \partial_y \left\{ \frac{\phi^2 (1 - \phi)^2}{\zeta} \left\{ \frac{\partial_y [G(\phi) W_{yy}]}{\phi} - \partial_y \frac{\delta F_h}{\delta \phi} + \partial_y [g(\phi) \partial_y^2 \phi] \right\} \right\}, \quad (7.5)$$

in which

$$\frac{\delta F_h}{\delta \phi} = f'(\phi) + \frac{1}{2} G'(\phi) [W_{yy} + W_{xx} - \ln(W_{yy} W_{xx} + W_{yy} + W_{xx} + 1 - W_{xy}^2)]. \quad (7.6)$$

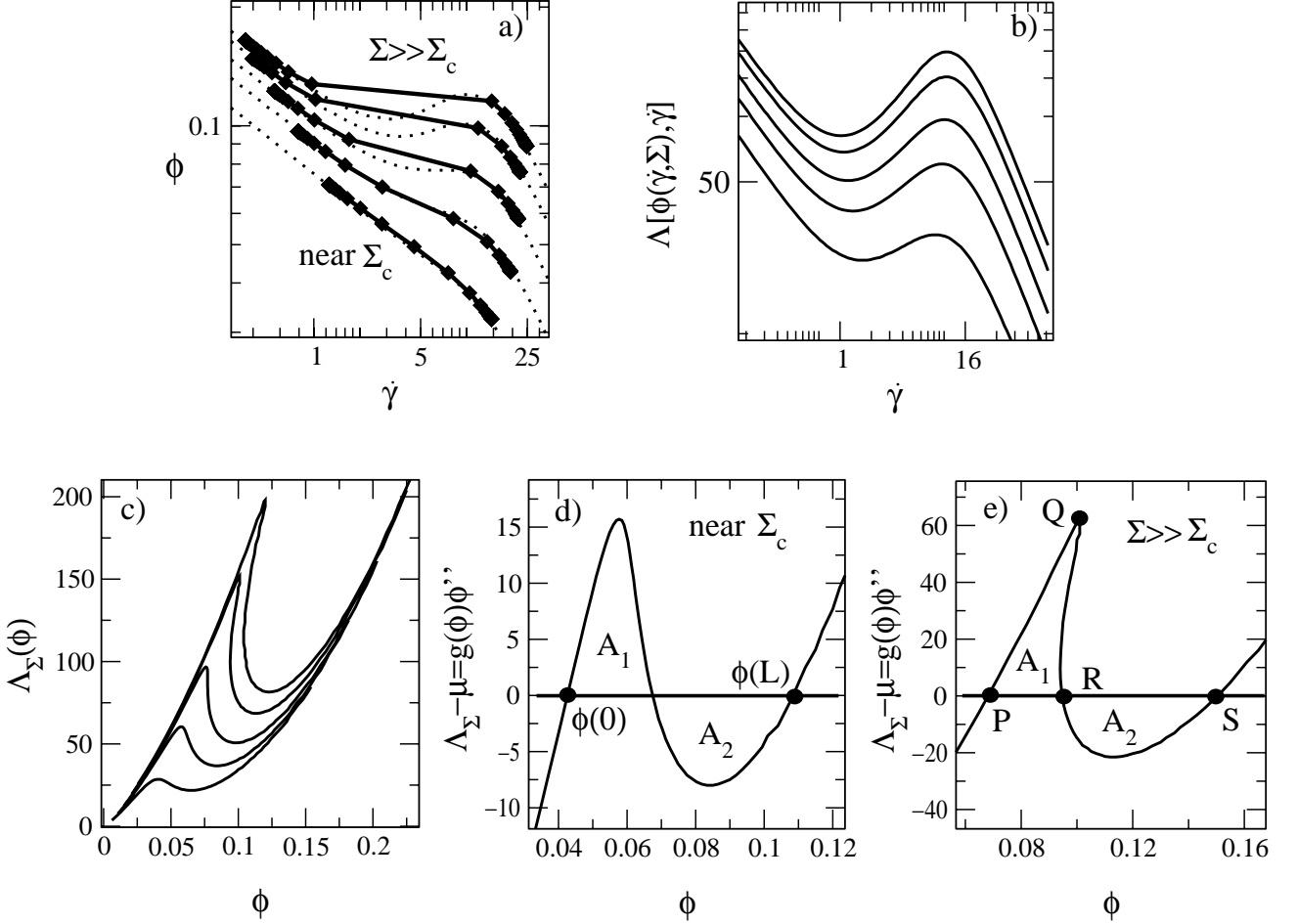


Fig. 16. (a) Dotted lines: relation between ϕ and $\dot{\gamma}$ for the case of a local constitutive equation, for several values of the shear stress, Σ , calculated using equations (7.3) and (7.4). Solid lines: the results of our numerics, showing that the ϕ -profile cannot properly negotiate the interface when $\mu(\dot{\gamma})$ is non-monotonic, as described in the main text. (b) The function Λ of equation (7.8) plotted *vs.* $\dot{\gamma}$ using the relation of (a). (c) Λ replotted *vs.* ϕ . (d) Λ *vs.* ϕ for a stress close to the critical point, where a smoothly banded state is allowed. A_1 and A_2 denote areas, with $A_1 \neq A_2$ in general, because of the integrating factor $1/g(\phi)$ in equation (7.11) (see text). (e) Λ *vs.* ϕ for a stress far from the critical point, where a smoothly banded state is not allowed (see text).

F_h is the homogeneous part of the free energy defined in Section 4.1 above. According to the usual definition, therefore, $\delta F_h / \delta \phi$ is the homogeneous chemical potential. Note, however, that it has a contribution from the non-linear effects of flow (the second term on the right-hand side (RHS) of Eq. (7.6)), beyond the usual equilibrium form, $f'(\phi)$. Integrating equation (7.5) twice, and using the boundary conditions $\partial_y \phi = 0$, $\partial_y^3 \phi = 0$, $\partial_y W_{\alpha\beta} = 0$ at $y = [0, L]$, we get

$$\mu = \Lambda(\phi, \dot{\gamma}) - g(\phi) \partial_y^2 \phi. \quad (7.7)$$

In this equation, μ is an integration constant, which is *not* equal to the chemical potential, because

$$\Lambda(\phi, \dot{\gamma}) = \frac{\delta F_h}{\delta \phi} - \frac{GW_{yy}}{\phi} + \int^{\dot{\gamma}} d\dot{\gamma}' \frac{1}{\phi^2} \frac{d\phi}{d\dot{\gamma}'} GW_{yy}, \quad (7.8)$$

with the second and third terms on the RHS arising from $\delta F / \delta \underline{W}$, not from $\delta F / \delta \phi$. Using the rela-

tions $\phi(\dot{\gamma}, \Sigma)$ of Figure 16(a), we numerically evaluated $\Lambda(\phi(\dot{\gamma}, \Sigma), \dot{\gamma})$ as a function of $\dot{\gamma}$ in Figure 16(b) for various values of Σ . We parametrically replotted $\Lambda_\Sigma(\phi)$ *vs.* ϕ in Figure 16(c) using $\dot{\gamma}$ as the plotting parameter. (Recall that ϕ and Λ are both single valued in $\dot{\gamma}$.) The doubling-back of $\Lambda_\Sigma(\phi)$ for large values of Σ is a direct consequence of the non-monotonicity of $\phi(\dot{\gamma}, \Sigma)$ *vs.* $\dot{\gamma}$ in this regime, in turn a consequence of the non-monotonicity of the intrinsic constitutive curve, described above.

The banded solution must therefore obey the single-variable problem

$$\mu = \Lambda_\Sigma(\phi) - g(\phi) \partial_y^2 \phi, \quad (7.9)$$

with boundary conditions

$$\partial_y \phi = 0 \quad \text{at } y = [0, L]. \quad (7.10)$$

Two features of the solution to equations (7.9) and (7.10) can easily be identified. First, multiplying equation (7.9)

across by $d\phi/dy$, integrating on ϕ , and imposing $\partial_y\phi = 0$ at the boundaries, we find

$$\int_{\phi(0)}^{\phi(L)} \frac{d\phi}{g(\phi)} [\Lambda_\Sigma(\phi) - \mu] = 0. \quad (7.11)$$

Second, the lengthscale of the banding interface is set by $[g(\phi)]^{1/2} \equiv \xi[\tilde{g}(\phi)]^{1/2}$. In the limit $\xi/L \rightarrow 0$, we have a narrow interface separating two bulk homogeneous phases, so that $\partial_y^n\phi = 0$ at $y = [0, L]$ for *all* $n = 1, 2, 3, \dots$. In particular,

$$\partial_y^2\phi \equiv \Lambda_\Sigma(\phi) - \mu = 0 \quad \text{at } y = [0, L]. \quad (7.12)$$

The constraints imposed by these equations (Eqs. (7.11) and (7.12)), are depicted graphically in Figs 16(d),(e). Because of the integrating factor $1/g(\phi)$, equation (7.11), does not quite give an “equal areas” construction ($A_1 \neq A_2$ in Figs. 16(d),(e)). However, equal areas could be recovered by the transformation $\phi \rightarrow s$ with $ds = d\phi/g(\phi)$. In our model $g(\phi)$ is a power law, so this transformation is just a stretching of the ϕ -axis by a scale factor that is monotonic in ϕ .

For a given imposed stress Σ close to the critical point, where the intrinsic constitutive curve is monotonic, the construction of Figure 16(d) uniquely specifies μ , $\phi(0)$ and $\phi(L)$ in the banded state. Through the local relation $\phi = \phi(\dot{\gamma}, \Sigma)$, $\dot{\gamma}(0)$ and $\dot{\gamma}(L)$ are also fixed. The fraction of the lower shear phase is also fixed via the lever rule $\bar{\phi} = \beta\phi(0) + (1 - \beta)\phi(L)$, since $\bar{\phi}$ is a fixed property of the system, specified externally. (We have assumed, without loss of generality, that the low shear phase is at the $y = 0$ side of the cell; band interchange is equivalent by symmetry considerations.) Finally, $\bar{\gamma}$ is fixed via $\bar{\gamma} = \beta\dot{\gamma}(0) + (1 - \beta)\dot{\gamma}(L)$. Thus, we have now shown that, under an imposed Σ and $\bar{\phi}$, the banded state is uniquely specified. (Recall, however, that in our numerics we imposed $\bar{\gamma}$, $\bar{\phi}$ and measured the subsequently selected Σ . We discuss this point in more detail in Sect. 7.3.3.)

For imposed stresses further from the critical point, where $\Lambda_\Sigma(\phi)$ doubles back on itself, the construction imposed by equations (7.11) and (7.12) (Fig. 16(e)) has a fundamental inconsistency that renders a smoothly banded state impossible. This can be seen as follows. Starting from the left-hand bulk homogeneous phase $y = 0, \phi = \phi(0)$ (point P in Fig. 16(e)), the system starts to cross through the interface to $\phi(L)$ (point S), following curve PQ. However the backward kink at Q means that ϕ must then start to decrease again. This is impossible, because the entire curve PQR has positive upward curvature, $\Lambda_\Sigma(\phi) - \mu \equiv g(\phi)\partial_y^2\phi > 0$. This inconsistency shows that a smoothly banded state cannot exist for stresses far above the critical point, because the number of kinks demanded by the non-monotonicity of Figure 16(a) is not allowed by the functional form of $\Lambda_\Sigma(\phi)$ (Fig. 16(c),(e)), which prescribes $\partial_y^2\phi$.

This argument is consistent with the fact that our numerics give sharp profiles in this regime, Figure 15(b). These profiles are replotted in Figure 16(a) (solid lines) in the $(\phi, \dot{\gamma})$ -plane. Each solution should have followed a

local (dotted) curve $\phi(\dot{\gamma})$, but instead has jumped across the region in which this curve is non-monotonic.

Recently, Yuan and Jupp numerically studied shear-induced demixing in a similar two-fluid Johnson-Segalman model, in two dimensions, (\hat{x}, \hat{y} in our notation) [44]. They presented results for the steady-state flow curves at two different concentrations, finding a non-analytic kink at the onset of shear banding, and an upwardly sloping banding stress plateau. Their simulation apparently gave unique state selection, even though interfacial terms were only present in the equation of motion for the concentration dynamics, and not in the viscoelastic constitutive equation. This interesting discrepancy between their work and ours deserves further investigation.

7.3.3 State selection revisited: Number of constraints vs. number of unknowns

In the previous section, we discussed state selection (when banding can occur, near the critical point) under an externally applied $\bar{\phi}$ and Σ . In our numerics, however, we actually applied $\bar{\phi}$ and $\bar{\gamma}$. In this section, therefore, we discuss state selection from a more general point of view, by balancing the number of unknowns in the banded state against the number of constraints. This will demonstrate that state selection can be obtained by fixing any two external control parameters.

The following parameters describe the banded state:

$$\bar{\phi}, \quad \bar{\gamma}, \quad \phi_\ell, \quad \phi_h, \quad \dot{\gamma}_\ell, \quad \dot{\gamma}_h, \quad \beta, \quad \mu, \quad \Sigma. \quad (7.13)$$

(β is the fraction of the gap occupied by the low-shear band.) Hence, we have nine parameters,

$$N_p = 9. \quad (7.14)$$

The model equations impose seven constraints on these parameters,

$$N_{c,\text{eqn}} = 7. \quad (7.15)$$

This can be seen as follows. First the local constitutive relation $\phi = \phi(\dot{\gamma}, \Sigma)$, applied to each phase, gives two constraints:

$$\phi_\ell = \phi(\dot{\gamma}_\ell, \Sigma) \quad \text{and} \quad \phi_h = \phi(\dot{\gamma}_h, \Sigma). \quad (7.16)$$

Two further constraints follow from the lever rules:

$$\bar{\phi} = \beta\phi_\ell + (1 - \beta)\phi_h \quad \text{and} \quad \bar{\gamma} = \beta\dot{\gamma}_\ell + (1 - \beta)\dot{\gamma}_h. \quad (7.17)$$

Finally, three more constraints follow from the construction

$$\int_{\phi(0)}^{\phi(L)} \frac{d\phi}{g(\phi)} [\Lambda_\Sigma(\phi) - \mu] = 0, \quad (7.18)$$

together with the requirement that for a narrow interface

$$\partial_y^2\phi = 0 \quad \text{at } y = 0, L, \quad (7.19)$$

which in turn sets

$$\Lambda_\Sigma(\phi) - \mu = 0 \quad \text{at } y = 0, L. \quad (7.20)$$

Hence, the number of constraints imposed by the model equations is 7, set against the 9 relevant parameters. Hence, we are free to constrain externally any two model parameters:

$$N_{c,\text{ext}} = N_p - N_{c,\text{eqn}} = 2. \quad (7.21)$$

For example, we can impose $\bar{\phi}$ and $\bar{\gamma}$ and the system will select the corresponding state Σ , μ , $\dot{\gamma}_\ell$, etc.

8 Conclusions

In this paper, we have studied the role of concentration coupling in the shear banding of complex fluids using the two-fluid, non-local Johnson-Segalman model. We have calculated phase diagrams for different degrees of coupling between concentration and mechanical degrees of freedom (molecular strain), and found a phase diagram qualitatively consistent with experiments on micellar solutions at concentrations well below the equilibrium isotropic-to-nematic transition [9]. Specific points to note are as follows.

1. The coexistence plateau in the steady-state flow curve slopes upward with shear rate, because of the concentration difference between the coexisting bands. The overall plateau height and width decrease with average concentration, terminating in a non-equilibrium critical point. CPCl/NaSal in brine [9] shows the same trend.
2. Of the two coexisting bands, the high-shear band has a smaller concentration due to the fact that concentration tends to move up gradients in the normal micellar strain component W_{yy} (where y is the flow-gradient direction). (W describes deformation relative to the unit tensor $\underline{\underline{\delta}}$, and W_{yy} is more negative in the high shear phase than in the lower shear phase.) Tie lines of the phase diagram in the $(\dot{\gamma}, \phi)$ -plane therefore have negative slope.
3. The concentration gap is smaller for smaller values of concentration coupling $\alpha \propto G'(\phi)/f''(\phi)$, and tends to zero in the limit $\alpha \rightarrow 0$. Accordingly, the coexistence region of the steady-state flow curve becomes flat in this limit.
4. We have explained how to reconstruct the flow phase diagram from the family of flow curves $\Sigma(\dot{\gamma}, \phi)$, measured for several average concentrations ϕ (Fig. 8). This reconstruction could be used to check new experimental measurements of concentration differences between the coexisting bands.
5. The phase diagram and flow curves depend slightly on the relative size of the interfacial term in the viscoelastic constitutive equation to that in the equation that specifies the concentration dynamics. This is a concrete demonstration of how stress selection and the coexistence conditions of driven systems depend on the nature of the interface, in contrast to equilibrium coexistence.

6. We find *no* unique state selection in the absence of gradient terms in the viscoelastic constitutive equation, except for stresses that are close to the critical point. This implies that, for a model to reproduce a uniquely selected stress, it is not enough simply to have gradient terms only in, for example, the concentration dynamics. If gradient terms were absent from the viscoelastic constitutive equation, one would expect, under certain conditions, no selection and hence a range of control parameters (shear stress or strain rate) for which the steady states are *intrinsically* history dependent. However, we expect that this will not be an issue in any real system, since viscoelastic gradient terms must always be present.
7. The interface width diverges at the critical point as a power law $(\Sigma - \Sigma_c)^{-n}$ with $n \approx 0.5$, although n differs slightly across the different order parameters.

Although our d-JS- ϕ model is highly oversimplified, we believe that it contains the basic ingredients required for a first description of wormlike micellar surfactant solutions at concentrations well below the isotropic-nematic (I-N) transition. In particular, it incorporates the minimal set of realistic degrees of freedom (tensorial order parameter for the micellar strain together with concentration), and unifies a non-monotonic flow curve with the Helfand-Fredrickson coupling between concentration and flow. Similar techniques could be applied to Cates' microscopic theory for wormlike micelles [1, 2].

We recall a previous calculation by Olmsted *et al.* for a solution of rigid rods near the I-N transition [41]. In future work we hope to unify these two approaches into a description of wormlike micelles that is valid over the entire concentration range. This should provide a first step towards understanding the crossover regime in the data of Figure 3, in which the coexistence plateau stress is a non-monotonic function of the micellar concentration.

We thank J.-F. Berret for the data in Figure 3, Paul Callaghan for useful discussions, and EPSRC GR/N11735 for financial support.

Appendix A. d-JS- ϕ equations in Cartesian coordinates

In this appendix, we give the components of the d-JS- ϕ model's equations for planar shear flow along the x -direction, allowing gradients only in the flow-gradient direction, y , as described in Section 4.3, above. The x -component of force-balance is (in the zero Reynolds limit considered in this paper)

$$0 = \partial_y [G(\phi) W_{xy}] + \eta_m \partial_y [\phi \partial_y v_{mx}] + \eta_s \partial_y [(1 - \phi) \partial_y v_{sx}]. \quad (\text{A.1})$$

The y -component of force-balance is fixed by incompressibility, $\nabla \cdot \underline{v} = 0$, along with the boundary condition $v_y = 0$:

$$0 = \phi v_{my} + (1 - \phi) v_{sy}. \quad (\text{A.2})$$

The relative velocity between the micelles and solvent (again ignoring inertial terms) is

$$v_{my} - v_{sy} = \frac{\phi(1-\phi)}{\zeta} \left\{ \frac{1}{\phi} \partial_y [G(\phi) W_{yy}] - \partial_y \frac{\delta F}{\delta \phi} - \partial_y [g(\phi) \partial_y^2 \phi] + 2 \frac{1}{\phi} \eta_m \partial_y [\phi \partial_y v_{my}] - 2 \frac{1}{1-\phi} \eta_s \partial_y [(1-\phi) \partial_y v_{sy}] \right\} \quad (\text{A.3})$$

in which

$$\frac{\delta F}{\delta \phi} = f'(\phi) + \frac{1}{2} G'(\phi) [W_{yy} + W_{xx} - \ln(W_{yy} W_{xx} + W_{yy} + W_{xx} + 1 - W_{xy}^2)], \quad (\text{A.4})$$

and

$$v_{mx} - v_{sx} = \frac{\phi(1-\phi)}{\zeta} \left\{ \frac{1}{\phi} \partial_y [G(\phi) W_{xy}] + \frac{1}{\phi} \eta_m \partial_y [\phi \partial_y v_{mx}] - \frac{1}{1-\phi} \eta_s \partial_y [(1-\phi) \partial_y v_{sx}] \right\}. \quad (\text{A.5})$$

The evolution of the micellar strain tensor is given by

$$\partial_t W_{xy} + v_{my} \partial_y W_{xy} = \frac{1}{2}(a-1) W_{xx} \partial_y v_{mx} + \frac{1}{2}(1+a) W_{yy} \partial_y v_{mx} + a W_{xy} \partial_y v_{my} + \partial_y v_{mx} - \frac{W_{xy}}{\tau(\phi)} + \frac{l(\phi)^2 \partial_y^2 W_{xy}}{\tau(\phi)}, \quad (\text{A.6})$$

$$\partial_t W_{yy} + v_{my} \partial_y W_{yy} = (a-1) W_{xy} \partial_y v_{mx} + 2a W_{yy} \partial_y v_{my} + 2 \partial_y v_{my} - \frac{W_{yy}}{\tau(\phi)} + \frac{l(\phi)^2 \partial_y^2 W_{yy}}{\tau(\phi)}, \quad (\text{A.7})$$

$$\partial_t W_{xx} + v_{my} \partial_y W_{xx} = (1+a) W_{xy} \partial_y v_{mx} - \frac{W_{xx}}{\tau(\phi)} + \frac{l(\phi)^2 \partial_y^2 W_{xx}}{\tau(\phi)}. \quad (\text{A.8})$$

Finally, the concentration dynamics are

$$\partial_t \phi = -\partial_y \left\{ \frac{\phi^2 (1-\phi)^2}{\zeta} \left\{ \frac{\partial_y [G(\phi) W_{yy}]}{\phi} - \partial_y \frac{\delta F_h}{\delta \phi} + \partial_y [g(\phi) \partial_y^2 \phi] + \frac{2 \eta_m \partial_y [\phi \partial_y v_{my}]}{\phi} - \frac{2}{1-\phi} \eta_s \partial_y [(1-\phi) \partial_y v_{sy}] \right\} \right\}. \quad (\text{A.9})$$

Appendix B. Stationary homogeneous solutions of the d-JS- ϕ model

In planar shear, the stationary homogeneous solutions to equations (4.7–4.9) for given $\dot{\gamma}$ and ϕ are $\underline{v}_{\text{rel}} \equiv \underline{v}_m - \underline{v}_s = 0$

$$W_{xy} = \frac{\dot{\gamma} \tau(\phi)}{1 + b \dot{\gamma}^2 \tau^2(\phi)}, \quad (\text{B.1a})$$

$$W_{yy} = \frac{a-1}{1+a} W_{xx} = -\frac{1}{(1+a)} \frac{b \dot{\gamma}^2}{1 + b \dot{\gamma}^2}, \quad (\text{B.1b})$$

$$W_{zz} = W_{xz} = W_{yz} = 0, \quad (\text{B.1c})$$

where $b = 1 - a^2$.

References

1. M.E. Cates, J. Phys. Chem. **94**, 371 (1990).
2. N.A. Spenley, M.E. Cates, Macromolecules **27**, 3850 (1994).
3. N.A. Spenley, M.E. Cates, T.C.B. McLeish, Phys. Rev. Lett. **71**, 939 (1993).
4. J. Yerushalmi, S. Katz, R. Shinnar, Chem. Engin. Sci. **25**, 1891 (1970).
5. P.D. Olmsted, O. Radulescu, C.-Y.D. Lu, J. Rheology **44**, 257 (2000).
6. C.-Y.D. Lu, P.D. Olmsted, R.C. Ball, Phys. Rev. Lett. **84**, 642 (2000).
7. P.D. Olmsted, C.-Y.D. Lu, Phys. Rev. E **56**, 55 (1997).
8. N.A. Spenley, X.F. Yuan, M.E. Cates, J. Phys. II **6**, 551 (1996).
9. J.F. Berret, D.C. Roux, G. Porte, J. Phys. II **4**, 1261 (1994).
10. P.T. Callaghan, M.E. Cates, C.J. Rofo, J.B.A.F. Smeulders, J. Phys. II **6**, 375 (1996).
11. C. Grand, J. Arrault, M.E. Cates, J. Phys. II **7**, 1071 (1997).
12. R.W. Mair, P.T. Callaghan, Europhys. Lett. **36**, 719 (1996).
13. R.W. Mair, P.T. Callaghan, Europhys. Lett. **65**, 241 (1996).
14. M.M. Britton, P.T. Callaghan, Phys. Rev. Lett. **78**, 4930 (1997).
15. J.F. Berret, D.C. Roux, G. Porte, P. Lindner, Europhys. Lett. **25**, 521 (1994).
16. V. Schmitt, F. Lequeux, A. Pousse, D. Roux, Langmuir **10**, 955 (1994).
17. E. Cappelaere, J.F. Berret, J.P. Decruppe, R. Cressely, P. Lindner, Phys. Rev. E **56**, 1869 (1997).
18. H. Rehage, H. Hoffmann, Mol. Phys. **74**, 933 (1991).
19. J.P. Decruppe, R. Cressely, R. Makhloufi, E. Cappelaere, Colloid Polym. Sci. **273**, 346 (1995).
20. R. Makhloufi, J.P. Decruppe, A. Aitali, R. Cressely, Europhys. Lett. **32**, 253 (1995).
21. J.P. Decruppe, E. Cappelaere, R. Cressely, J. Phys. II **7**, 257 (1997).
22. J.F. Berret, G. Porte, J.P. Decruppe, Phys. Rev. E **55**, 1668 (1997).
23. S. Lerouge, J.P. Decruppe, J.F. Berret, Langmuir **16**, 6464 (2000).
24. J.F. Berret, D.C. Roux, P. Lindner, Eur. Phys. J. B **5**, 67 (1998).
25. V. Schmitt, C.M. Marques, F. Lequeux, Phys. Rev. E **52**, 4009 (1995).
26. F. Brochard, P.-G. de Gennes, Macromolecules **10**, 1157 (1977).

27. E. Helfand, G.H. Fredrickson, *Phys. Rev. Lett.* **62**, 2468 (1989).
28. M. Doi, A. Onuki, *J. Phys. II* **2**, 1631 (1992).
29. S.T. Milner, *Phys. Rev. E* **48**, 3674 (1993).
30. X.L. Wu, D.J. Pine, P.K. Dixon, *Phys. Rev. Lett.* **66**, 2408 (1991).
31. A.N. Beris, V.G. Mavrantzas, *J. Rheol.* **38**, 1235 (1994).
32. T. Sun, A.C. Balazs, D. Jasnow, *Phys. Rev. E* **55**, R6344 (1997).
33. H. Tanaka, *Phys. Rev. Lett.* **76**, 787 (1996).
34. J.P. Decruppe, S. Lerouge, J.F. Berret, *Phys. Rev. E* **63**, 022501 (2001).
35. S.M. Fielding, P.D. Olmsted, to be published in *Phys. Rev. Lett.*, preprint cond-mat/0207344.
36. S.M. Fielding, P.D. Olmsted, submitted to *Phys. Rev. E*, preprint cond-mat/0208599.
37. M. Johnson, D. Segalman, *J. Non-Newton. Fluid Mech.* **2**, 255 (1977).
38. S.T. Milner, *Phys. Rev. Lett.* **66**, 1477 (1991).
39. P.-G. de Gennes, *Macromolecules* **9**, 587 (1976).
40. F. Brochard, *J. Phys. (Paris)* **44**, 39 (1983).
41. P.D. Olmsted, C.-Y.D. Lu, *Phys. Rev. E* **60**, 4397 (1999).
42. The derivative $\phi \nabla \delta F / \delta \phi$ in equations (4.8) and (4.7) actually contains not only the osmotic free energy, but also the elastic free energy (second term in Eq. (4.3)). This leads to an extra elastic force on the micelles. However, this does not affect the qualitative trends, and we do not discuss it further.
43. N. Clarke, T.C.B. McLeish, *Phys. Rev. E* **57**, R3731 (1998).
44. X.-F. Yuan, L. Jupp, *Europhys. Lett.* **60**, 691 (2002).
45. D.S. Malkus, J.S. Nohel, B.J. Plohr, *J. Comp. Phys.* **87**, 464 (1990).
46. D.S. Malkus, J.S. Nohel, B.J. Plohr, *SIAM J. Appl. Math.* **51**, 899 (1991).
47. R.W. Kolkka, D.S. Malkus, M.G. Hansen, G.R. Ierley, R.A. Worthing, *J. Non-Newton. Fluid Mech.* **29**, 303 (1988).
48. P.D. Olmsted, P.M. Goldbart, *Phys. Rev. A* **46**, 4966 (1992).
49. J.K.G. Dhont, *Phys. Rev. E* **60**, 4534 (1999).
50. X.F. Yuan, *Europhys. Lett.* **46**, 542 (1999).
51. A.W. El-Kareh, L.G. Leal, *J. Non-Newton. Fluid Mech.* **33**, 257 (1989).
52. J.L. Goveas, G.H. Fredrickson, *Eur. Phys. J. B* **2**, 79 (1998).
53. M. Criado-Sanchez, D. Jou, J. Casas-Vasquez, L.F. del Castillo, *Phys. Rev. E* **66**, 061803 (2002).
54. F. Bautista, J.F.A. Soltero, E.R. Macías, J.E. Puig, O. Manero, *J. Phys. Chem. B* **106**, 13018 (2002).
55. T.A.J. Lenstra, Z. Dogic, J.K.G. Dhont, *J. Chem. Phys.* **114**, 10151 (2001).
56. J.F. Berret, D.C. Roux, G. Porte, *J. Phys. II* **4**, 1261 (1994).
57. We use the fact that the drag is large to set $v_{mx} - v_{sx} = 0$ to corrections $O(1/\zeta)$ (Eq. (A.5)), so that $\partial_y v_{mx} = \partial_y v_{sx} = \dot{\gamma}$.